Modeling mechanochemical coupling in cell polarity establishment

Ondrej Maxian

October 23, 2023

This project is about understanding the design principles by which cells combine mechanics (the actomyosin network) and biochemistry to robustly polarize.

1   Myosin and CDC-42

We begin by considering a model of myosin by itself, to determine if it can spontaneously polarize. Spontaneous polarization of myosin, if possible, would explain the maintenance-phase rescue experiments that we observe.

1.1   Myosin as a self-patterning material

Let us begin by building a toy model for myosin dynamics. This section is a summary of the paper [2], which considers the same problem. The novelty in what we do will come later, when we couple myosin to branched actin and other proteins.

We describe the dynamics of myosin $M(x,t)$ using the advection-diffusion equation

$$\partial_t M + \partial_x \left(vM \right) = D_M \partial_x^2 M. \tag{1}$$

The complication is that the myosin is advected through a velocity field of its own making. The velocity field comes from stress generated in the fluid,

$$\sigma = \eta \partial_x v + \sigma_a(M), \tag{2}$$

which is a combination of viscous stress and active stress. As in [2], we ignore the elastic part of the stress, assuming the actomyosin cortex is purely viscous when in reality it is visco-elastic. The force balance equation in the fluid says that the force due to stress must be balanced by the drag force,

$$\gamma v = \partial_x \sigma, \tag{3}$$

where γ is the drag coefficient. Combining the force balance (3) with the stress expression (2) gives an auxillary equation for the velocity field

$$\gamma v = \eta \partial_x^2 v + \partial_x \sigma_a(M) \tag{4}$$

which couples to the myosin equation (1) via the active stress.

The advection-diffusion equation (1) is mass-preserving, meaning that the uniform steady state is just given by $M_0 = \frac{1}{L} \int_0^L M(x,0)\, dx$. For the active stress, we let $\sigma_a = \sigma_0 \hat{\sigma}_a(M)$. The analysis of [2] shows that (for periodic boundary conditions) the uniform steady state is unstable when

$$\mathrm{Pe} \times \frac{M_0 \left(\partial_M \hat{\sigma}_a\left(M_0\right)\right)}{1 + (2\pi \ell/L)^2} > 1, \tag{5}$$

where $\ell = \sqrt{\eta/\gamma}$ is the characteristic lengthscale over which velocity decays (the diffusive length-scale for velocity), L is the system length, and the Peclet number

$$\mathrm{Pe} = \frac{\sigma_0}{D_M \gamma} \tag{6}$$

expresses the ratio of advective transport to diffusive transport. Qualitatively, the system has a uniform steady state and a second peaked steady state, where advective flux into the peaks matches the diffusive flux into the peaks. For this steady state to be stable, the advective transport must be sufficiently large relative to diffusive transport, so the Peclet number must be sufficiently large.

1.2 Myosin pattern formation with turnover

We now introduce a single species model of myosin with turnover,

$$\partial_t M + \partial_x (vM) = D_M \partial_x^2 M + k_M^{\mathrm{on}} M_{\mathrm{cyto}} - k_M^{\mathrm{off}} M \tag{7a}$$

$$\gamma v = \eta \partial_x^2 v + \partial_x \sigma_a(M) \tag{7b}$$

It will be useful to nondimensionalize this equation, using the scalings

$$x = \hat{x}L \qquad t = \hat{t}/k_M^{\mathrm{off}} \qquad Y = \hat{Y}Y^{(\mathrm{Tot})} \qquad v = \hat{v}\frac{\sigma_0}{\sqrt{\eta\gamma}} \tag{8}$$

The resulting equations are

$$\partial_{\hat{t}}\hat{M} + \hat{\sigma}_0 \partial_{\hat{x}}\left(\hat{v}\hat{M}\right) = \hat{D}_M \partial_{\hat{x}}^2 \hat{M} + \hat{K}_M^{\mathrm{on}}\left(1 - \int_0^1 \hat{M}(x)\, dx\right) - \hat{M} \tag{9a}$$

$$\hat{v} = \hat{\ell}^2 \partial_{\hat{x}}^2 v + \hat{\ell}\partial_{\hat{x}}\hat{\sigma}_a(\hat{M}) \tag{9b}$$

2

Parameter	Description	Value	Units	Ref	Notes
L	Domain length	134.6	μm	[4]	radii 27×15 μm ellipse
h	Cytoplasmic "thickness"	9.5	μm	[4]	(area/circumference)
D_M	Myosin diffusivity	0.05	μm^2/s	[5]	
k_M^{on}	Myosin attachment rate	0.5	μm/s		Fit to get 30% bound myosin
k_M^{off}	Myosin detachment rate	0.12	1/s	[5]	
$M^{(\text{Tot})}$	Maximum bound myosin density	2600	#/μm	[5]	3.5×10^5 molecules/(134.6 μm)
η	Cytoskeletal fluid viscosity	0.1	Pa·s		$100 \times$ water
γ	Myosin drag coefficient	10^{-3}	Pa·s/μm^2		$\ell = \sqrt{\eta/\gamma} = 10\,\mu$m [5]
σ_0	Stress coefficient and form	0.0042	Pa		Fit in Sec. 1.2.1
$\hat{\sigma}_a(\hat{M})$	Stress function of myosin	$\hat{M}$			Fit in Sec. 1.2.1

Table 1: Parameter values for myosin model. All of these parameters listed with a citation are lifted directly from the corresponding paper. Remaining parameters: the on rate k_M^{on} is chosen to give 30% bound myosin [5, Fig. S3], as opposed to exact repitition of the value in [5, Fig. 1(d)]. Later this rate will change in the presence of CDC-42. We make an assumption about the fluid viscosity η, which then gives us the drag coefficient γ from $\ell = 10$ μm [5]. The remaining parameters are fit in Section 1.2.1 from the wild-type data of [13]. These parameters are all checked.

and are controlled by the dimensionless parameters

$$\hat{\sigma}_0 = \left(\frac{\sigma_0/\sqrt{\eta\gamma}}{L k_M^{\text{off}}} \right) \qquad \hat{D}_M = \frac{D_M}{k_M^{\text{off}} L^2} \qquad \hat{K}_M^{\text{on}} = \frac{k_M^{\text{on}}}{h k_M^{\text{off}}} \qquad \hat{\ell} = \frac{\sqrt{\eta/\gamma}}{L}. \tag{10}$$

Recalling that $1/k_M^{\text{off}}$ is the residence time, these dimensionless parameters can be understood in the following way:

1. $\hat{\sigma}_0$ is the fraction of the domain that active transport occurs on before a myosin molecule jumps off. To see this, note that residence time $\times$ the advective velocity $\sigma_0/\sqrt{\eta\gamma}$ is the amount of motion, which is normalized by the domain length.

2. $\hat{D}_M$ is the maximum fraction of the domain a molecule diffuses before it unbinds (in the extreme case when the gradient in the domain is $1/L$, the diffusive velocity is D_M/L).

3. $\hat{K}_M^{\text{on}}$ is the ratio of the binding rate to unbinding rate when all the molecules are cytoplasmic. The uniform steady state of the model is given by $\hat{M}_0 = \hat{K}_M^{\text{on}} / \left(1 + \hat{K}_M^{\text{on}} \right)$.

4. $\hat{\ell}$ is the ratio of the hydrodynamic lengthscale to the domain length.

Prior to performing linear stability analysis, we need to first determine the function σ_a. We do this in the next section by fitting experimental data.

1.2.1 Inferring flow profile from experiments

Because we can measure the cortical velocity and myosin intensity, we can actually infer the function $\sigma_a(M)$ in dimensional units from the experimental data [13]. We in particular isolate the myosin intensity and flow speed during "late maintenance" phase in wild type embroys [13, Fig. 1B(bottom)], plotting the results in the top panels of Fig. 1. In the top left plot, we plot the myosin intensity, normalized so that the mean amount of bound myosin is 0.3, in accordance with wild-type measurements in [5, Fig. S3].

In the top right plot, we show the velocity in μm/min. In both cases, the data are plotted on $\hat{x} \in [0.25, 0.75]$, which corresponds to half of the embryo (one of the lines going from anterior to posterior end). We then periodically extend this data so that we fill the whole circumference $\hat{x} \in [0, 1]$; these are the blue lines in Fig. 1. Finally, to remove the noise from our measurements (e.g., the strange dips in the myosin concentration at the anteior and posterior pole), we fit the periodized version with a two-term (+constant) Fourier representation, which gives the red lines in Fig. 1.

To extract the stress profile from the smoothed velocity and myosin intensity, we consider a hybrid dimensional form of (7b)

$$\gamma v - \frac{\eta}{L^2}\partial_{\hat{x}}^2 v = \frac{1}{L}\partial_{\hat{x}}\sigma_a(M).$$

Let the Fourier series representation for $v(\hat{x}) = \sum_k \tilde{v}(k) \exp(2\pi i k \hat{x})$, and likewise for $\hat{\sigma}_a$. Then, in Fourier space, the solution for σ_a is given by

$$\sigma_a(k) = \frac{\gamma + \eta/L^2 \, (2\pi k)^2}{2\pi i k/L}\tilde{v}(k). \tag{11}$$

The $k = 0$ mode is undefined because σ_a only appears differentiated; we therefore set it such that the real space stress has a minimum value of zero.

We plug the parameters from Table 1 into (11) and show the resulting real space stress in the bottom left panel of Fig. 1. This is the dimensional stress σ_a. In the right panel of Fig. 1, we normalize and shift the stress so that it has the same mean and range as the myosin profile $\hat{M}$. Obtaining the same range allows us to read off the constant $\sigma_0 = 4.2 \times 10^{-3}$ Pa that controls the magnitude of the advective flows. In particular, the dimensionless parameter $\hat{\sigma}_0$ defined in (10) is
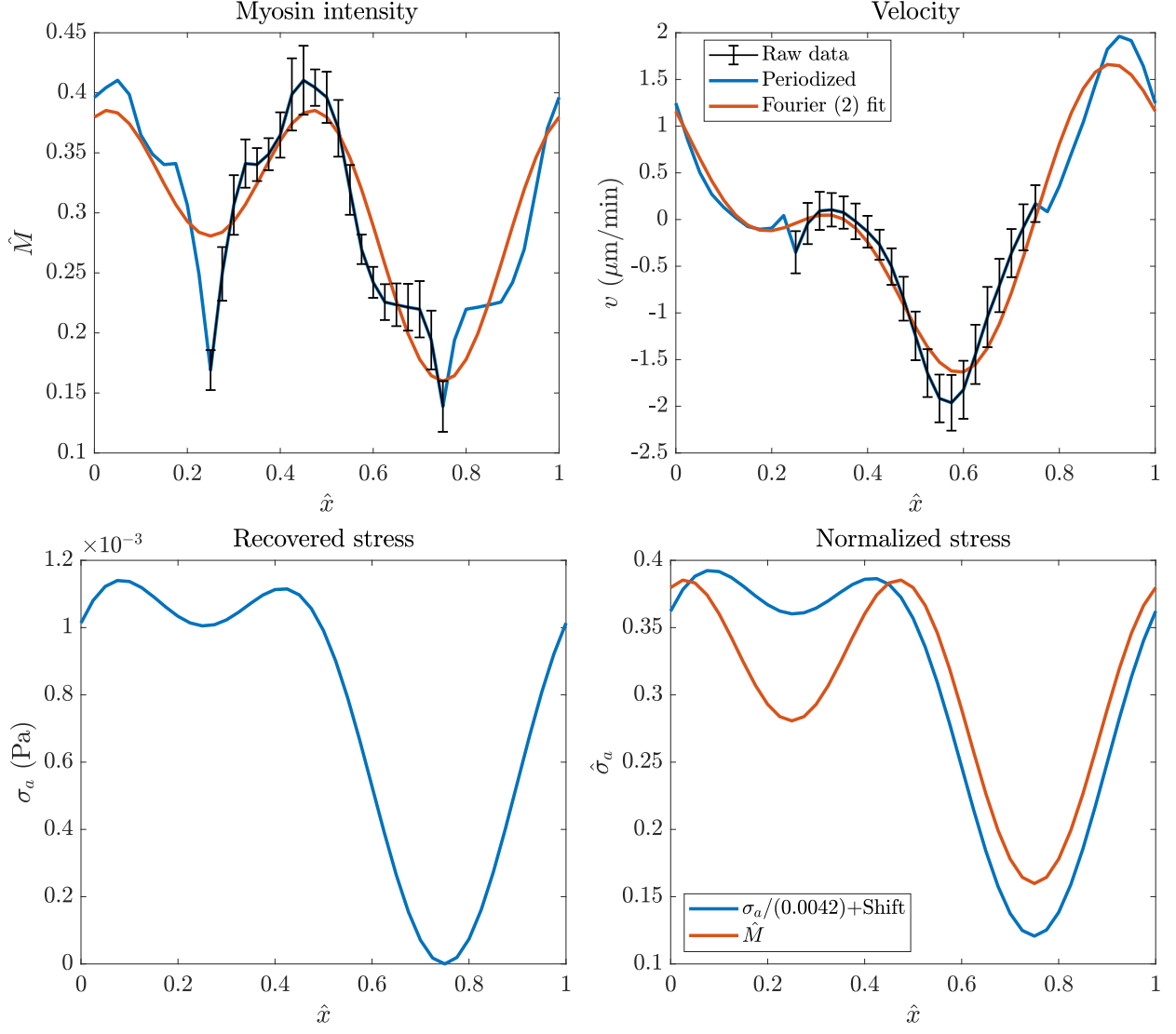
Figure 1: Extracting the velocity profile and active stress from wild-type embryos. Top: the experimental data for myosin intensity (left) and velocity in μm/min (right). We show the raw data in black (which goes from anterior to posterior), the periodized version in blue, and a two-term (three terms if we include the constant) Fourier series representation in red. Bottom left: the recovered stress profile $\sigma_a(\hat{x})$ in dimensional units. Bottom right: comparing the recovered stress to the myosin intensity, after normalizing by $\sigma_0 = 0.0011$ Pa. It is clear that, roughly speaking, $\hat{\sigma}_a = \hat{M}$, or at least that this is a reasonable approximation.
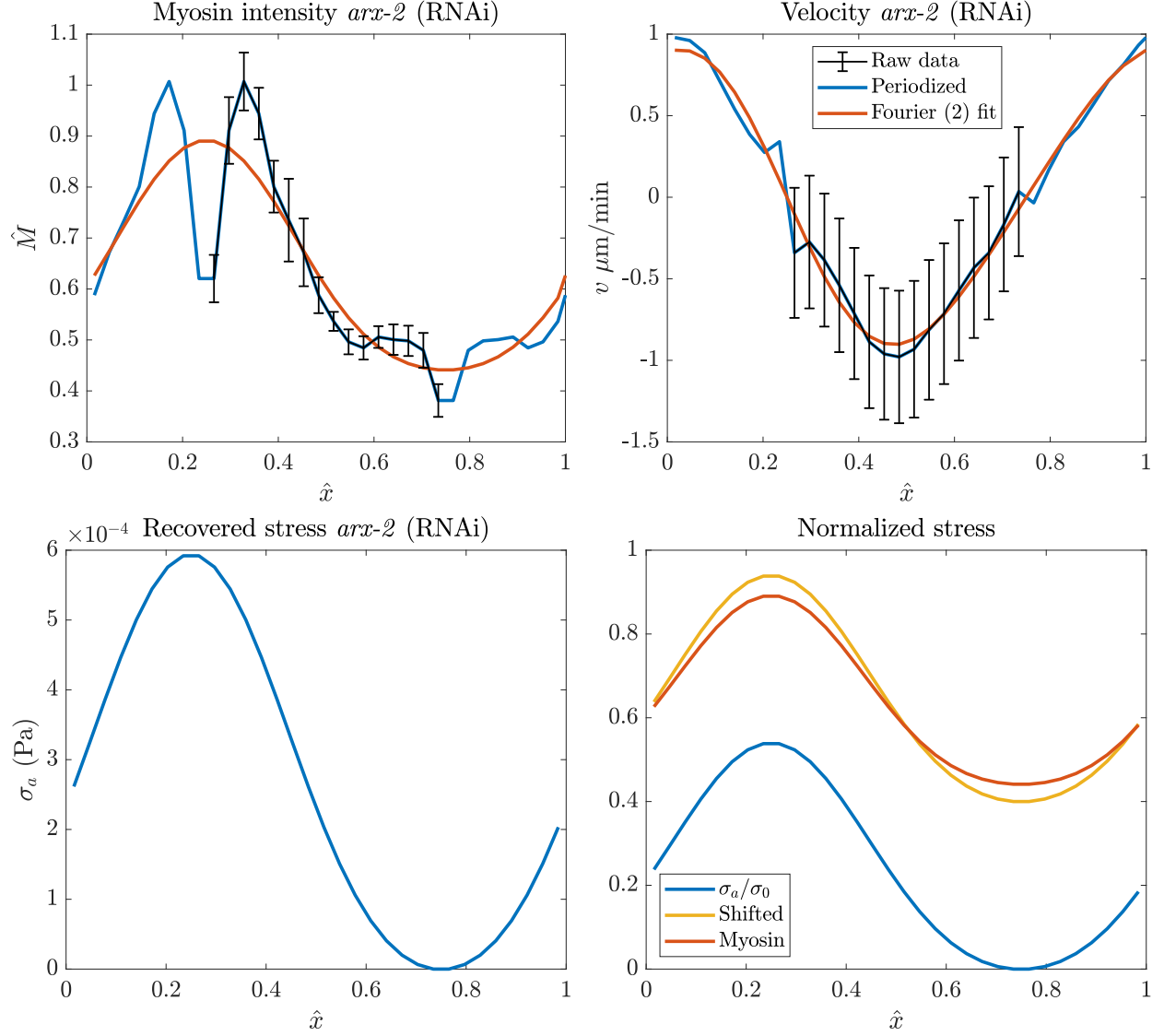
Figure 2: Same plot as Fig. 1, but in *arx-2* (RNAi) embryos. In the bottom right plot, we normalize by $\sigma_0 = 1.1 \times 10^{-3}$ Pa. This makes the stress (when shifted by an arbitrary constant) roughly the same as the myosin profile (also normalized so its maximum is 1). COME BACK TO THIS LATER, SEEING IF WE CAN GET CORRECT $\hat{M}$.

seen to be equal to

$$\hat{\sigma}_0 = \left(\frac{\sigma_0/\sqrt{\eta\gamma}}{Lk_M^{\text{off}}} \right) = 0.026. \tag{12}$$

In additiom, the bottom right panel of Fig. 1, also shows that we can roughly set

$$\hat{\sigma}_a = \hat{M} \tag{13}$$

as a good approximation to the stress. The function itself is ambiguous, since $\hat{M} = 0.3$ defines two different values of the stress depending on the side of the domain, but $\hat{\sigma}_a = \hat{M}$ appears to be a good approximation.

We confirm this in Fig. 2, where we repeat the velocity fitting procedure in *arx-2* (RNAi) embryos, which lack branched actin and consequently have a simpler velocity profile. We extract the stress profile in the bottom left plot in exactly the same way as in wild-type. Then, to compute normalize stress we divide out by $\hat{\sigma}_0 = 1.1 \times 10^{-3}$ Pa (obtained from wild-type). The normalize stress, when shifted by an arbitrary constant, lines up almost perfectly with the smoothed myosin profile, demonstrating that our rough approach from wild-type embryos extends to other embryos as well. Thus, this section gives us $\sigma_a = \left(1.1 \times 10^{-3} \right) \hat{M}$.

1.2.2   Linear stability analysis

We now perform linear stability analysis using the experimentally-fitted stress profile. The uniform steady state is $\hat{M}_0 = \hat{K}_M^{\text{on}} / \left(1 + \hat{K}_M^{\text{on}} \right)$. We consider a perturbation around that state $\hat{M} = \hat{M}_0 + \delta\hat{M}$, where $\delta\hat{M} = \delta\hat{M}_0 e^{\lambda(k)\hat{t} + 2\pi ik\hat{x}}$. Plugging this into (9b), we get the velocity [2, Eq. (11)]

$$\hat{v} = \frac{2\pi ik\hat{\ell}\hat{\sigma}_a'(\hat{M}_0)}{1 + \left(2\pi k\hat{\ell} \right)^2} \hat{\delta}M. \tag{14}$$

Substituting this velocity into (9a), and considering only the first order terms, we get the following equation for the eigenvalues

$$\lambda(k) = \frac{4\pi^2 k^2 \hat{\ell}\hat{M}_0\hat{\sigma}_0\hat{\sigma}_a'(\hat{M}_0)}{1 + 4\pi^2 k^2\hat{\ell}^2} - \hat{D}_M 4\pi^2 k^2 - 1 \tag{15}$$

Using the parameters in Table 1, we have the following known values for the dimensionless groups

$$\hat{D}_M = 2.3 \times 10^{-5} \qquad \hat{M}_0 \approx 0.3 \qquad \hat{\sigma}_a' = 1 \qquad \hat{\ell} \approx 0.07 \tag{16}$$

This gives the dispersion relation shown in Fig. 3 for different values of $\hat{\sigma}_0$. We observe strong flow coupling required for instability; with $\hat{\sigma}_0 = 0.2$ (flow transports myosins around 20% of the cell before they come off), we still do not see any instability.

7
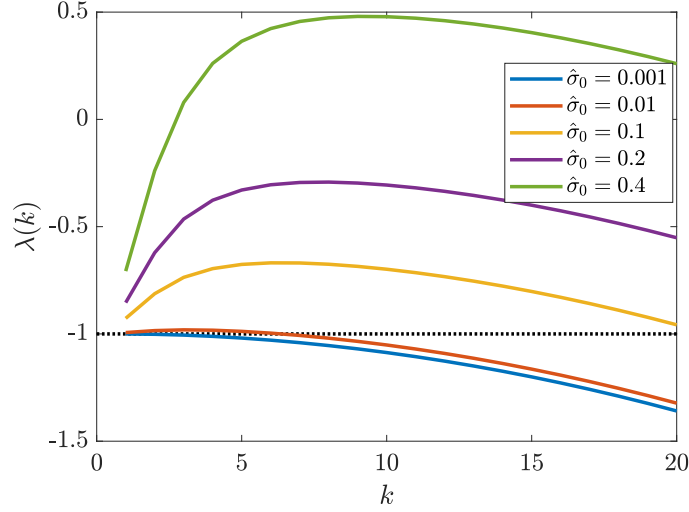
Figure 3: Dispersion relation (15) for myosin for different values of $\hat{\sigma}_0$. Positive eigenvalues indicate instability of the steady state. Dotted black line at $\lambda = -1$ reflects the axis of instability *without* unbinding kinetics.

Importantly, the -1 in the dispersion relation (15) comes from the unbinding kinetics; thus, unbinding, which happens proportional to the number of bound myosins, makes it *harder* to leave the steady state. Indeed, without the -1, the instability occurs at $\hat{\sigma}_0 \approx 10^{-3}$, which is pretty weak coupling to the flow. When we account for unbinding, diffusion becomes so small as to be irrelevant, as for the $k = 1$ mode the coefficient in (15) is $\hat{D}_M 4\pi^2 \approx 10^{-3}$. **Thus, the real balance here (to generate the instability) is not between advection and diffusion, but between advection and *unbinding*.** Specifically, the advective flow must be strong enough to overcome the increase in unbinding that happens in areas enriched in myosin. Considering that we already have seen wild-type embryos have $\sigma_0 \approx 0.004$, it is clear that myosin cannot self-polarize in the zygote.

2 Biochemistry of PAR-3 and PAR-2

We are motivated first by the experimental observations that asymmetries in the PAR proteins are stable once set up, even in the absence of contractility. This experimental observation tells us that there is an intrinsic bistability in the biochemical circuit, which switches from a uniform state to a polarized state. In later sections, the switch will occur under the influence of actomyosin flows, while in this section the initial conditions will be the only way to switch the steady profiles.

Unlike in budding yeast cells [11], there is no experimental evidence that *C. elegans* cells can spontaneously polarize, which means that the system is truly bistable. Traditionally, it has been speculated that the bistability comes from mutual inhibition of the aPAR and pPAR proteins [6, 15]. But translating this idea into equations becomes much harder than might be expected! Indeed, ODEs based on first-order mass action kinetics of aPAR-pPAR inhibition *do not* yield bistable dynamics under any choice of parameters [3]. Attempts to overcome this have used stoichiometric coefficients for the biochemical equations that guarantee bistability [4, 5] or included actomyosin flows designed to transport the aPARs [14]. Both of these approaches are grounded more in intuition than in biological evidence, as there is no reason to doubt mass action kinetics, and recent experiments have shown that both aPARs and pPARs are transported by myosin [7].

Recent experimental observations about PAR-3 provide a potential way out of this conundrum. Indeed, it was recently shown that PAR-3 asymmetries are stable even in the absence of all posterior inhibitors, which suggest that the dynamics of PAR-3 *by itself* are intrinsically bistable [8]. Experimental evidence has shown that the bistability occurs via a mechanism in which membrane-bound PAR-3 recruits additional cytoplasmic monomers to the membrane. One goal of this section is to translate these observations into equations which demonstrate how PAR-3 can set up and maintain an asymmetry in the absence of posterior inhibition. We then incorporate posterior PAR proteins and show how their inclusion modifies the dynamics of PAR-3, potentially shifting the boundary between the two protein domains.

2.1 Basic equations and framework for PAR-3

We first formulate our model of PAR-3 dynamics, which is based loosely on that of Lang and Munro [10]. The key property of PAR-3 that makes it different from other proteins is its ability to form *oligomers* on the membrane. Unlike monomers, these oligomers do not diffuse in the membrane, and are not found in high concentrations in the cytoplasm. Based on these experimental observations, we will consider a model in which there are two species of PAR-3,

1. Monomeric PAR-3, which can be found in cytoplasmic form (A_{cyto}) or membrane bound (A_1) form.

2. Oligomerized PAR-3 (A_n) which is only found on the membrane and can neither diffuse nor become unbound. These assumptions are approximations based on the experimental observations in [8, Fig. 3K], which show that the dissociation rate constant for dimers in

trimers is 5–10 times smaller than that for monomers, and also the experimental observation that PAR-3 only binds to the membrane in monomer form [8].

Given these assumptions, the model equations in dimensional form are as follows

$$\partial_t A_1 = D_A \partial_x^2 A_1 + \left(k_A^{\text{on}} + k_A^+ f_A^+ \left(A_1 + 2A_n\right)\right) A_{\text{cyto}} + 2k_A^{\text{dp}} A_n - 2k_A^{\text{p}} A_1^2 - k_A^{\text{off}} A_1 \tag{17a}$$

$$\partial_t A_n = k_A^{\text{p}} A_1^2 - k_A^{\text{dp}} A_n \tag{17b}$$

$$A_{\text{cyto}} = \frac{1}{hL} \left(A^{(\text{Tot})} L - \int_0^L \left(A_1(x) + 2A_n(x)\right) dx \right) \tag{17c}$$

A complete list of parameters with units and values is given in Table 2, but it will be helpful to point out the important ones in our model. First, the feedback strength k_A^+, which has units of length/time, gives the rate at which cytoplasmic PAR-3 is recruited to the membrane. It is multiplied by the dimensionless flux function f_A^+, which gives the dimensionless strength of recruitment as a function of the total bound PAR-3. The overall on rate is proportional to the cytoplasmic concentration, which is defined in (17c). There $A^{(\text{Tot})}$ expresses the density of bound PAR-3 when all molecules are bound to the membrane (units 1/length). Subtracting the amount of bound PAR-3 and dividing by the membrane area gives the cytoplasmic concentration in units of 1/area.

2.1.1 Dimensionless form

A sensible timescale for the system is the time a given PAR-3 molecule spends on the membrane. Because about 80% of the bound PAR-3 molecules are in oligomer form, and since the depolymerization reaction is much slower than the unbinding reaction, we nondimensionalize time by $1/k_A^{\text{dp}}$. This gives the dimensionless (hatted) variables defined by

$$x = \hat{x}L \qquad t = \hat{t}/k_A^{\text{dp}} \qquad Y = \hat{Y}Y^{(\text{Tot})}.$$

Substituting into (17) gives the rewritten dynamics

$$\partial_{\hat{t}} \hat{A}_1 = \hat{D}_A \partial_{\hat{x}}^2 \hat{A}_1 + \hat{K}_A^{\text{on}} \left(1 + \hat{K}_A^+ f_A^+ \left(\hat{A}_1 + 2\hat{A}_n\right)\right) \left(1 - \int_0^1 \left(\hat{A}_1(x) + 2\hat{A}_n(x)\right) d\hat{x}\right)$$
$$+ 2\hat{K}_A^{\text{dp}} \hat{A}_n - 2\hat{K}_A^{\text{p}} \hat{A}_1^2 - \hat{K}_A^{\text{off}} \hat{A}_1 \tag{18a}$$

$$\partial_{\hat{t}} \hat{A}_n = \hat{K}_A^{\text{p}} \hat{A}_1^2 - \hat{K}_A^{\text{dp}} \hat{A}_n \tag{18b}$$

$$\hat{D}_A = \frac{D_A}{L^2 k_A^{\text{dp}}}, \quad \hat{K}_A^{\text{on}} = \frac{k_A^{\text{on}}}{k_A^{\text{dp}} h}, \quad \hat{K}_A^+ = \frac{k_A^+}{k_A^{\text{on}}}, \quad \hat{K}_A^{\text{off}} = \frac{k_A^{\text{off}}}{k_A^{\text{dp}}}, \quad \hat{K}_A^{\text{p}} = \frac{k_A^{\text{p}} A^{(\text{Tot})}}{k_A^{\text{dp}}}, \quad \hat{K}_A^{\text{dp}} = 1 \tag{18c}$$

10

2.1.2 Linear feedback model

We first look at the dynamics of PAR-3 with the linear feedback model

$$f_A^+(x) = x,$$

similar to what was used by Lang and Munro [10]. The uniform steady state for A_1 can be found by first solving (18b) at steady state to obtain

$$A_n = \frac{\hat{K}_A^{\mathrm{p}}}{\hat{K}_A^{\mathrm{dp}}} \hat{A}_1^{\,2}. \tag{19}$$

Substituting this into (18a), we get a quartic equation for A_1 at steady state

$$0 = \hat{K}_A^{\mathrm{on}} \left(1 + \hat{K}_A^+ \left(\hat{A}_1 + 2\frac{\hat{K}_A^{\mathrm{p}}}{\hat{K}_A^{\mathrm{dp}}} \hat{A}_1^{\,2}\right)\right) \left(1 - \left(\hat{A}_1 + 2\frac{\hat{K}_A^{\mathrm{p}}}{\hat{K}_A^{\mathrm{dp}}} \hat{A}_1^{\,2}\right)\right) - \hat{K}_A^{\mathrm{off}} \hat{A}_1,$$

which is just a polynomial and can be solved numerically. This quartic equation is controlled by three parameters: $\hat{K}_A^{\mathrm{on}}/\hat{K}_A^{\mathrm{off}}$, $\hat{K}_A^{\mathrm{p}}/\hat{K}_A^{\mathrm{dp}}$, and $\hat{K}_A^+$. A simple scan of these three parameters on the range $[0.01, 100]$ shows that this equation has a single real root in the range $[0, 1]$. We denote the steady state as $\bar{\hat{A}}_1$ and $\bar{\hat{A}}_n$.

2.1.3 Linear stability analysis

We now need to determine if the uniform steady state is stable. To do this, we consider a perturbation $\delta \hat{A}_1$ and $\delta \hat{A}_n$ with $\int_0^1 \delta \hat{A}_1(x)\, dx = \int_0^1 \delta \hat{A}_n(x)\, dx = 0$. The resulting linearized equations for the kth Fourier mode of A_1 and A_n can be written as

$$\frac{d}{dt} \begin{pmatrix} \hat{A}_1^{(k)} \\ \hat{A}_n^{(k)} \end{pmatrix} = \begin{pmatrix} -\hat{K}_A^{\mathrm{off}} + \bar{\hat{A}}_c \hat{K}_A^+ \hat{K}_A^{\mathrm{on}} - 4\bar{\hat{A}}_1 \hat{K}_A^{\mathrm{p}} - 4\pi^2 k^2 \hat{D}_A & 2\left(\hat{K}_A^{\mathrm{dp}} + \bar{\hat{A}}_c \hat{K}_A^+ \hat{K}_A^{\mathrm{on}}\right) \\ 2\bar{\hat{A}}_1 \hat{K}_A^{\mathrm{p}} & -\hat{K}_A^{\mathrm{dp}} \end{pmatrix} \begin{pmatrix} \hat{A}_1^{(k)} \\ \hat{A}_n^{(k)} \end{pmatrix}$$

$$\bar{\hat{A}}_c = 1 - \bar{\hat{A}}_1 - 2\bar{\hat{A}}_n$$

As such, the uniform steady state is unstable when the determinant of this matrix (with $k = 1$)

$$\hat{K}_A^{\mathrm{dp}}(\hat{K}_A^{\mathrm{off}} + 4\pi^2 \hat{D}_A) - \bar{\hat{A}}_1 \hat{K}_A^{\mathrm{dp}} \hat{K}_A^+ \hat{K}_A^{\mathrm{on}} - 4\bar{\hat{A}}_1 \bar{\hat{A}}_c \hat{K}_A^+ \hat{K}_A^{\mathrm{on}} \hat{K}_A^{\mathrm{p}} < 0$$

$$\hat{K}_A^+ \hat{K}_A^{\mathrm{on}} \left(\bar{\hat{A}}_1 \hat{K}_A^{\mathrm{dp}} + 4\bar{\hat{A}}_1 \bar{\hat{A}}_c \hat{K}_A^{\mathrm{p}}\right) > \hat{K}_A^{\mathrm{dp}}(\hat{K}_A^{\mathrm{off}} + 4\pi^2 \hat{D}_A) \tag{20}$$

Although this equation is somewhat misleading because $\bar{\hat{A}}_1$ is a function of the other parameters, it gives us the following observations, some of which are immediate, and some of which we determined numerically:

1. The uniform steady state can always be made stable by making the diffusion sufficiently fast.

2. Conversely, the uniform steady state can be made unstable by increasing the feedback $\hat{K}_A^+$.

3. In contrast to how it appears in (20), it turns out that the steady state is stable for *higher* values of $\hat{K}_A^{\text{on}}$, because of cytoplasmic depletion. Specifically, if there is so much protein bound at the uniform steady state, there will not be any more to be recruited to destabilize it. So the uniform steady state is actually unstable when $\hat{K}_A^{\text{on}}$ is sufficiently *small* so as to leave enough cytoplasmic protein. As such, this parameter is not really that interesting to study going forward.

4. For a fixed amount of membrane-bound protein, having more in the oligomerized state (either by increasing $\hat{K}_A^{\text{p}}$ or decreasing $\hat{K}_A^{\text{dp}}$) assists in making the uniform state unstable because oligomers can't diffuse and thus diffusion is effectively slower.

2.1.4 Parameters

To effectively constrain the model, we need values for at least some of the parameters. Table 2 provides a start to this by listing the parameters which are known definitively from experimental observations. It leaves three parameters which are not directly known: the on rate k_A^{on}, the polymerization rate k_A^{p}, and the feedback strength k_A^+. This is of course in addition to the feedback function f_A^+, which we here assume to be linear.

To obtain parameters which are unknown, we will first assume that the feedback is small, and fit the observations to the posterior side of wild-type embryos. If we assume that the total PAR-3 concentration is roughly maximum in the anterior half, then the posterior side will have $\hat{A}_1 + 2\hat{A}_n = 0.2$ [8, Fig. 2], and roughly 30% of the PAR-3 is in oligomer form [8] (this comes from $\alpha = 0.42$ as the expononent for the exponential distribution on the posterior side). We then look for values of k_A^{on} and k_A^{p} that give these values, finding $k_A^{\text{on}} = 1$ μm/s and $k_A^{\text{p}} = 0.03$ μm/s. These leaves us k_A^+ as a control knob for the dynamics.

To obtain the total amount of each PAR protein and myosin (or at least the correct range), we work off the measurements in [5, Fig. S3]. There it was reported that there are roughly 350×10^3 molecules of myosin in the cell, and about 200×10^3 PAR proteins (150,000 PAR-2 and 250,000 PAR-3, but we will average these together and assume all proteins are in the same amount). To obtain a "maximum" from these values, we divide by the domain length of 134.6 μm. For the PAR proteins, we obtain 1486/μm, which we round to 1500/μm. For myosin, we obtain 2600/μm.

Parameter	Description	Value	Units	Ref	Notes
D_A	Monomeric PAR-3 diffusivity	0.1	$\mu m^2/s$	[8]	
D_P	PAR-2 diffusivity	0.15	$\mu m^2/s$	[4]	
k_A^{on}	Monomeric PAR-3 attachment rate	1	$\mu m/s$	FIT	20% attached no feedback [8, Fig. 2]
k_P^{on}	Monomeric PAR-2 attachment rate	0.13	$\mu m/s$	[5]	
k_A^{off}	Monomeric PAR-3 detachment rate	3	$1/s$	[8]	(Fig. 3K)
k_P^{off}	PAR-2 detachment rate	7.3×10^{-3}	$1/s$	[5]	
k_A^+	PAR-3 self recruitment rate	?	$\mu m/s$		Control knob for PAR-3
k_A^{p}	PAR-3 polymerization rate	0.03	$\mu m/s$	[8]	30% monomers no feedback [8, Fig. 3G]
k_A^{dp}	PAR-3 depolymerization rate	0.08	$1/s$	[8]	Fig. 4E therein
r_{AP}	Rate of PAR-2 inhibition by PAR-3	6×10^{-4}	$\mu m/s$		Match experiments [16, Fig. 5B]
r_{PA}	Rate of PAR-3 inhibition by PAR-2	6×10^{-4}	$\mu m/s$		Same as r_{AP}
$A^{(Tot)}$	Maximum bound PAR-3 density	1500	$\#/\mu m$	[5]	Same for all PARs
$P^{(Tot)}$	Maximum bound PAR-2 density	1500	$\#/\mu m$		Same for all PARs

Table 2: Additional parameter values for PAR-3 and PAR-2 model. Update the code to reflect this! And check every parameter again

2.1.5 Results

With these parameters set, the dimensionless parameters in (18c) are given as

$$\hat{D}_A = 2.8 \times 10^{-4}, \quad \hat{K}_A^{on} = 2.7, \quad \hat{K}_A^+ = \frac{k_A^+}{k_A^{on}}, \quad \hat{K}_A^{off} = 37.5, \quad \hat{K}_A^{p} = 18.8, \quad \hat{K}_A^{dp} = 1$$

and so the parameter $\hat{K}_A^+$ provides a control knob by which we can study the system.

We begin our study by looking at the stability of the uniform state. In Fig. 4 (top plot), we examine the steady states and their stability as a function of the feedback parameter K_A^+. As the feedback increases, more oligomers are found in steady state. The limit to this is when there are about 75% oligomers, at which point the steady state becomes unstable. The bottom plot shows a further analysis of the stability. When the feedback is small enough ($\hat{K}_A^+ = 2$), perturbations around the steady state tend to drive the dynamics back to it, while for larger feedback ($\hat{K}_A^+ = 4$) perturbations are amplified. We note that what has to be considered for the stability analysis is *not* the absolute attachment rate (dotted blue), but the attachment rate *with the steady state cytoplasmic concentration.* This is because perturbations do not affect the cytoplasmic concentration (or do so only weakly).

What do the dynamics look like when we perturb around the steady state for different feedback
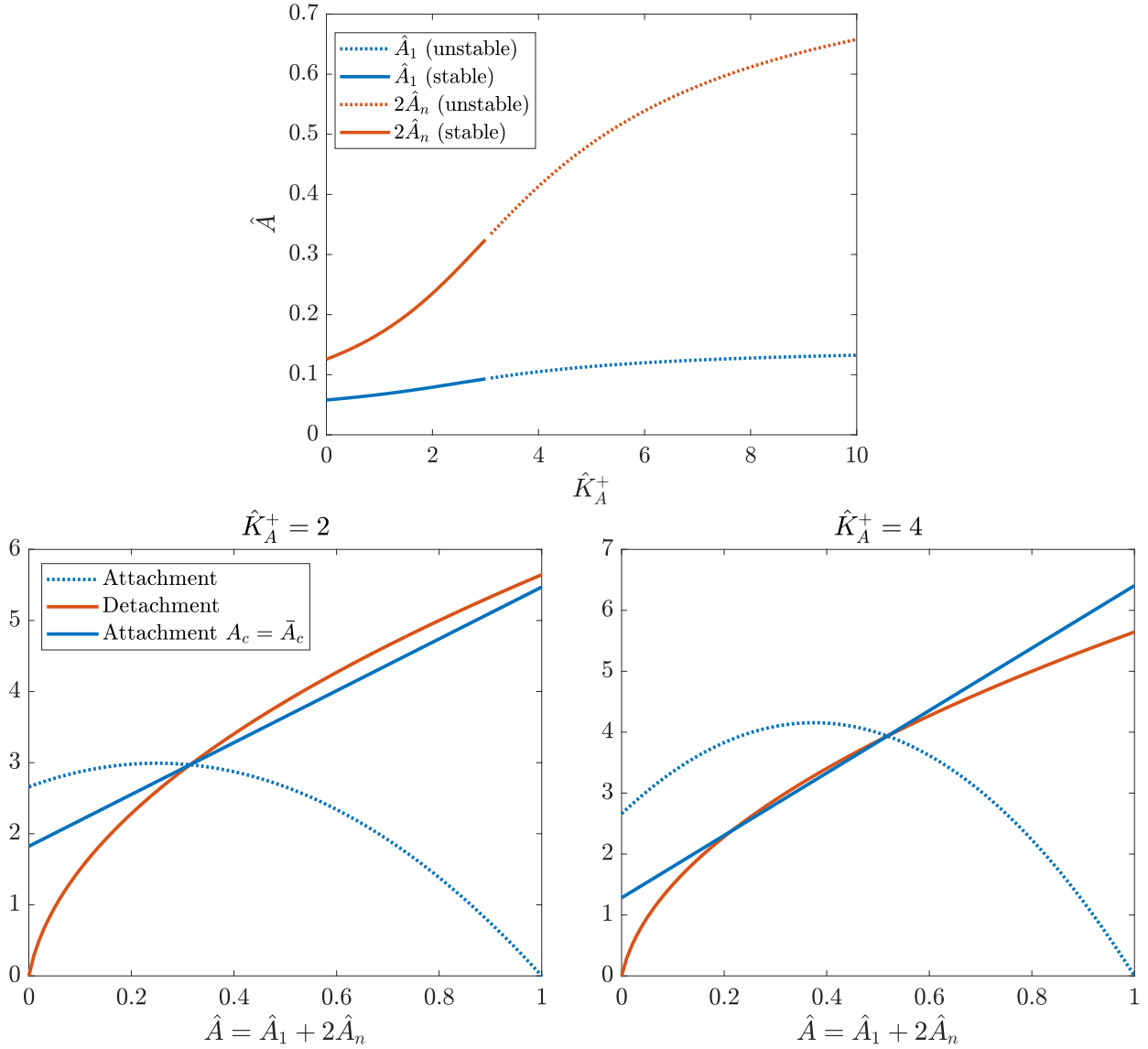
Figure 4: Steady states for the PAR-3 model **with linear feedback** as a function of dimensionless feedback strength. (Top:) The steady state bound monomer and oligomer proportion as a function of the feedback strength K_f^+. The blue line is the concentration of monomeric PAR-3, while the red is the concentration of oligomers. The solid lines represent stable steady states, while the dotted lines are unstable ones. (Bottom:) Flux plane analysis for the stable (left) and unstable (right) case. The stability analysis is determined by how the attachment rate (solid blue line, with constant cytoplasmic concentration) compares to the detachment rate (red) near the steady state.
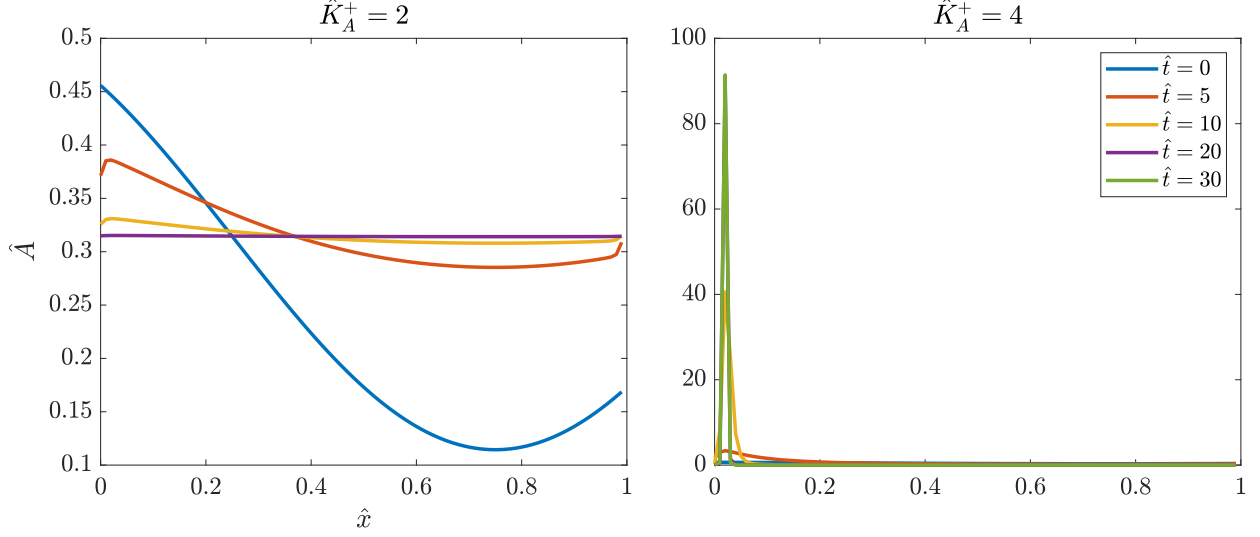
Figure 5: Dynamics of the PAR-3 model with linear feedback. We plot the dynamics using the same initial condition and two different choices of the feedback strength: $K_A^+ = 2$ (left) and $K_A^+ = 4$ (right). We plot time in units of k_A^{dp}, so $\hat{t} = 1$ corresponds to 12.5 seconds of real time (thus $\hat{t} = 30$ corresponds to about 10 minutes).

strengths? In Fig. 5, we plot the dynamics using different colored lines with the same initial condition and two different choices of the feedback strength: $\hat{K}_A^+ = 2$ (which is expected to be stable) and $\hat{K}_A^+ = 4$ (unstable). We plot time in units of k_A^{dp}, so $\hat{t} = 1$ corresponds to 12.5 seconds of real time (thus $\hat{t} = 30$ corresponds to 10 minutes). We observe stable dynamics when $\hat{K}_A^+ = 2$ as expected, as the initially perturbed profile decays down to the uniform steady state. When $\hat{K}_A^+ = 4$, however, the dynamics are extreme, as the steady state is a very narrow peak which is limited by diffusion and depletion of the cytoplasmic pool. Since most of the monomers are in oligomer form, diffusion is almost zero, which makes the peak grow until the cytoplasmic pool is depleted.

We note that the growth of the peak is a point of disagreement between this work and that of Lang and Munro [10]. In that study, it was argued that the shift in the boundary is relatively slow, on the order of a hundred seconds per micron. So how can we explain the observations in Fig. 5, which show a more rapid shift in the boundary? The answer lies in the amount of available cytoplasmic protein. Our experiments are based on perturbations from *steady state*, where some 40% of the PAR-3 is bound and 60% is available in the cytoplasm. But the numerical experiments in [10, Fig. 4D] begin with a state where all of the protein is bound at time zero, which prevents the feedback from kicking in as rapidly, and gives a slower movement of the boundary.

No matter the initial condition, it is clear that the linear feedback model with large enough

feedback strength develops a polarized state spontaneously, and in this case the region that contains more PAR-3 always outcompetes the region that contains less. This results in pulse-like shocks which don't slow down until the cytoplasmic pool is depleted. This contradicts the main experimental observation we want to explain, which is that PAR-3 can be stably enriched in half of the cortex, without contractility and without posterior PARs. The main reason for the contradiction is the feedback model: because we assume feedback proportional to monomer concentration, the feedback can only increase once the state is unstable. In the next section, we experiment with a nonlinear feedback model which gives results closer to the experiments.

2.2 PAR-3 model with feedback fit to experimental results

In the previous section, we saw that a linear feedback model for PAR-3 cannot explain the experimental data that shows stable enrichment of PAR-3 on one side of the cortex. The reason for this is that there is no cap to the feedback, and so it continues to concentrate protein until the cytoplasmic pool is depleted.

There are really three key experimental observations that give us a hint as to the stability portrait of the PAR-3 dynamics:

1. The spatially uniform state is stable (for at least 10 minutes) in the absence of contractility.

2. The polarized state is stable once set up, even without contractility. That is, *at constant cytoplasmic concentration there are two stable steady states.*

3. Let u be the concentration of the uniform state. Then, at the polarized state, without pPAR inhibition the concentration at the anterior end is (roughly) $1.25u$ and $0.125u$ at the posterior end.

The key here is observation 2, which gives us important information about the flux plane. In particular, it tells us that the attachment rate has to equal the detachment rate (at constant cytoplasmic concentration) *three times*, with two giving stable steady states (and necessarily a middle one giving an unstable steady state). Since the detachment rate in this model is fixed, this observation essentially tells us what the feedback function should look like.

Let's see if a feedback function with a cap can match these observations. Specifically, we suppose that
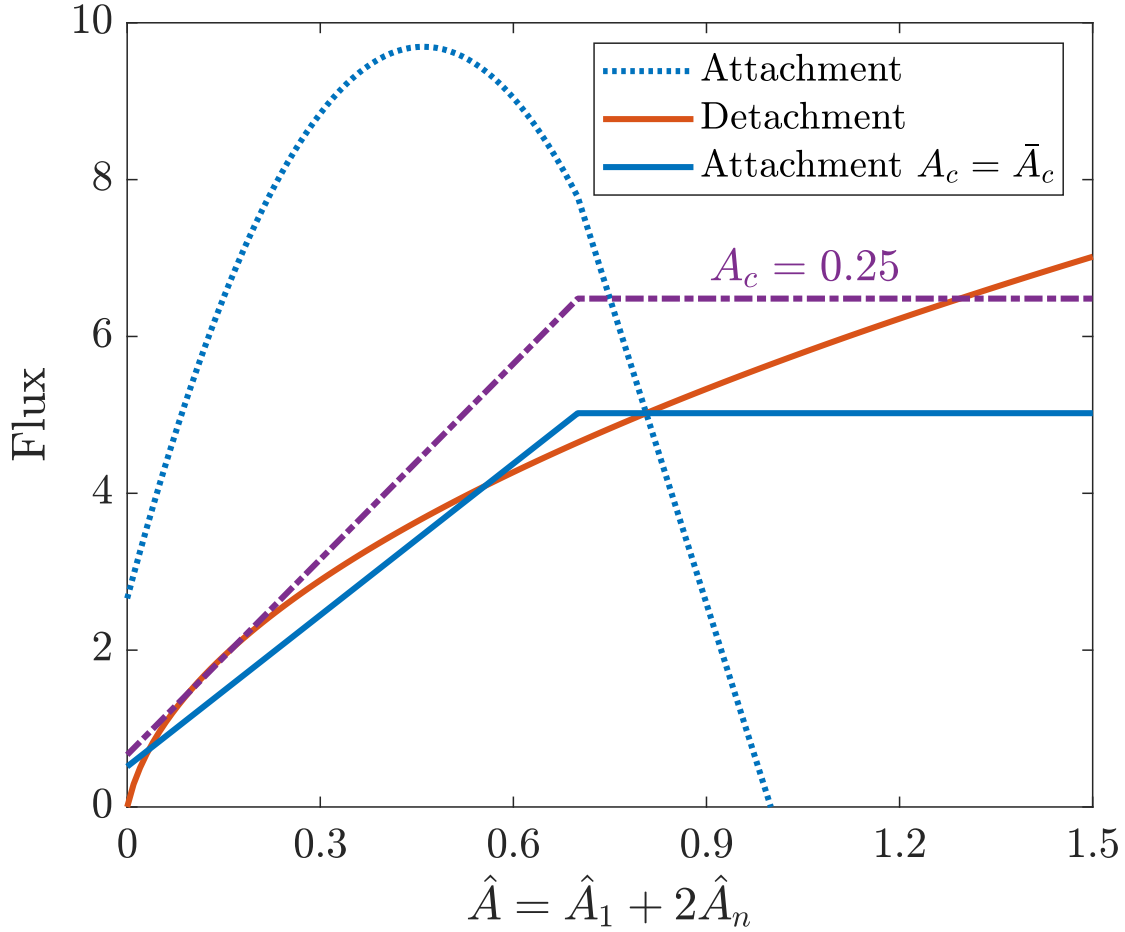
$$f_A^+(x) = \min\left(x, f_{\max}\right),$$
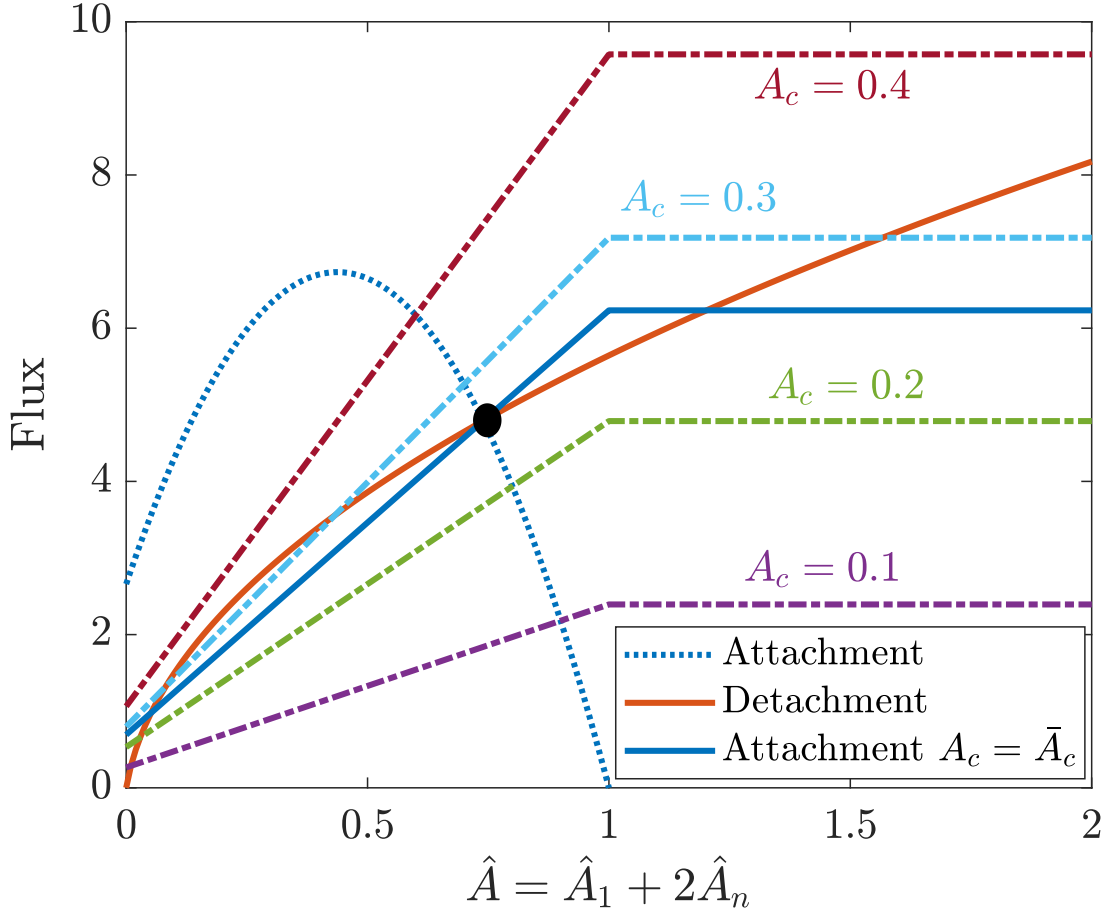
Figure 6: Flux plane with $f_{\max} = 1$ and $\hat{K}_A+ = 8$. We plot the attachment flux (assuming uniform concentration) as dotted blue, the detachment flux as solid red, and the attachment flux at the steady state cytoplasmic concentrated in solid blue. The dashed-dotted lines show different values of the cytoplasmic concentration. The black dot shows the uniform steady state.

which should limit the growth of unstable boundaries. Figure 6 provides an example of how this might work, where we set the feedback $\hat{K}_A^+ = 8$ so that the steady state sits near $\hat{A} = 0.8$, and $f_{\max} = 1$. The uniform steady state is unstable (because the attachment flux exceeds the detachment flux near it), but the cap on the feedback makes the instability self-limiting, so that advances in the concentration will stall near $\hat{A} = 1.3$ (solid blue line meets solid red line). Unfortunately, because the feedback cap sits at 1, the uniform steady state will always be unstable. Because the uniform state is limited by 1, the attachment will always grow linearly there, which exceeds the rate of growth of detachment.

To remedy this problem, we need *the feedback to be saturated at the uniform steady state.* To

Figure 7: Flux plane with $f_{\max} = 0.7$ and $\hat{K}_A+ = 12.5$. We plot the attachment flux (assuming uniform concentration) as dotted blue, the detachment flux as solid red, and the attachment flux at the steady state cytoplasmic concentrated in solid blue. The dashed-dotted lines show different values of the cytoplasmic concentration. The black dot shows the uniform steady state.

do this, we adjust the parameters slightly so that $f_{\max} = 0.7$. To get a uniform steady state around $\hat{A} = 0.8$, we set $\hat{K}_A^+ = 12.5$. The resulting flux plane is shown in Fig. 7. There we see a *stable* steady state with $\hat{A} = 0.8$, and this is the only uniform steady state (dotted blue line and solid red line meet exactly once). The purple line shows what happens when we adjust the cytoplasmic concentration upwards to $\hat{A}_c = 0.25$; in this case there emerge two steady states, one with $\hat{A} \approx 1.25$ and one with $\hat{A} \approx 0.1$. These new steady states are a consequence of the increased cytoplasmic concentration.

In order for these to be truly steady states, then we let y be the position of the boundary. Then
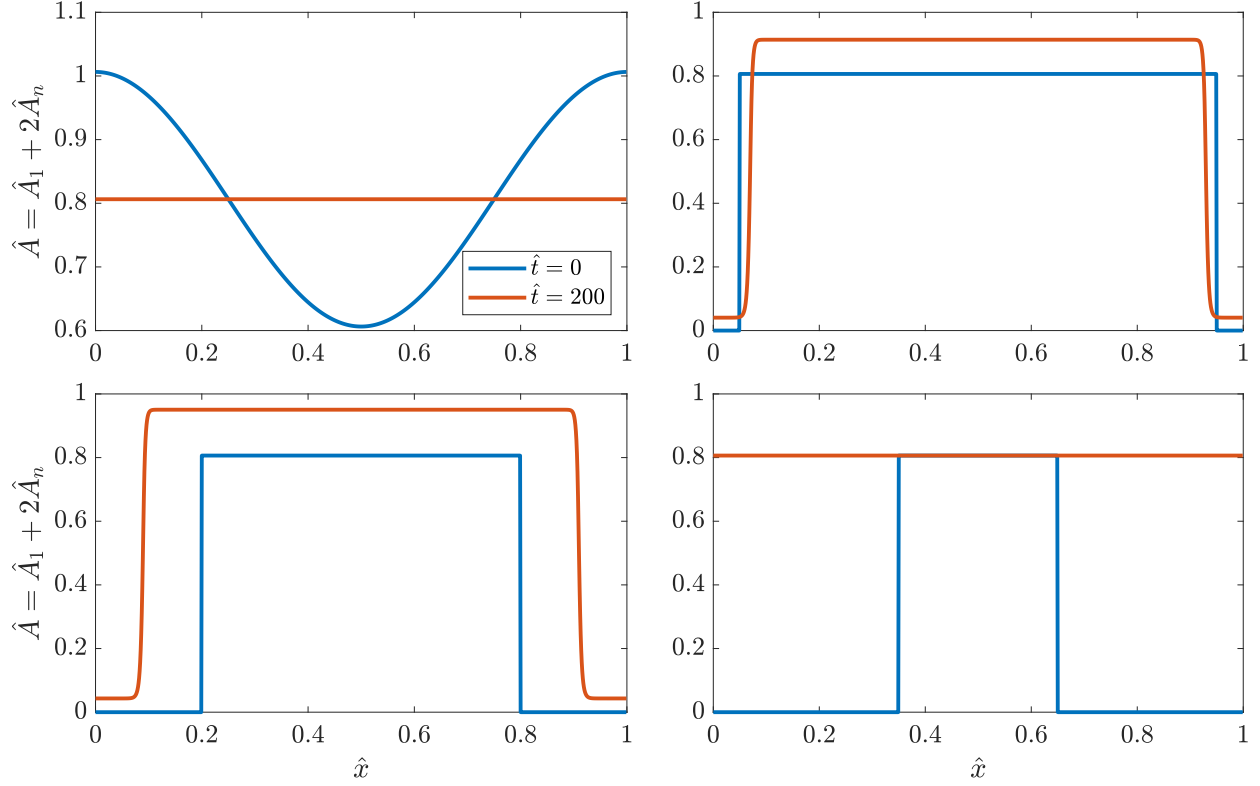
Figure 8: Simulating the PAR-3 feedback model with $\hat{K}_A^+ = 12.5$ and $f_{\max} = 0.7$. Top plot: steady states from initial profiles. The initial states are shown in blue, and the final states are shown in red. The system can maintain an asymmetry for cytoplasmic concentration in a range near the uniform state.

in the absence of diffusion, if the equation

$$(1 - y)\hat{A}_1(A_c) + y\hat{A}_2(A_c) = 1 - A_c \tag{21}$$

has a solution, then y defines the boundary position. Otherwise, there will be a uniform state.

2.2.1 Results

Let's now see how the model performs when we fix $\hat{K}_A^+ = 12.5$ and $f_{\max} = 0.7$, so that the stability portrait is as shown in Fig. 7. In Figure 8, we show initial and final distributions of PAR-3. In the top left plot, we see that the uniform steady state is stable, as expected from the stability diagram. By contrast, when we introduce an asymmetry into the system by depleting PAR-3 in part of the domain, we see bistable dynamics where the small part gravitates to one steady state, while the larger end goes to another. In the bistable region, we observe a posterior concentration which is always roughly 5% of the anterior concentration. This is within the range reported by Sailer et al. for embryos lacking posterior PAR inhibition (3–15%) [13, Fig. 4C].

19
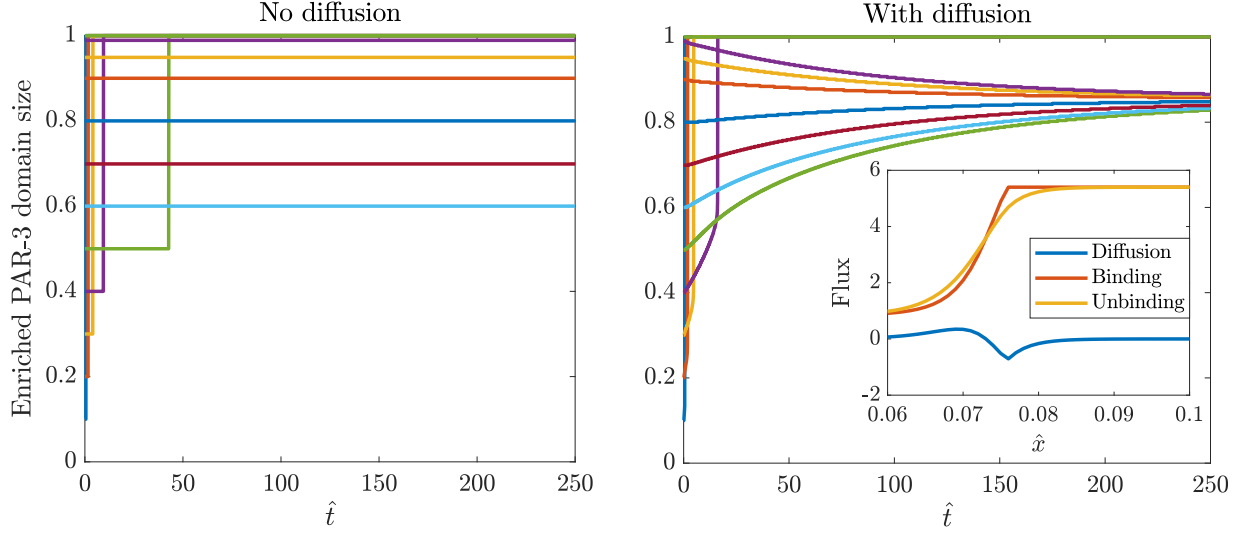
Figure 9: Size of PAR-3 domain over time without (left) and with (right) diffusion of monomeric PAR-3. Without diffusion, any boundary position with more than 50% enriched PAR-3 is stable, because there exists a solution to (21) where the on rate balances the off rate in both the enriched and depleted regions. When we introduce diffusion, there is an additional constraint in the boundary layer, as shown in the inset (which shows the steady state fluxes). This additional constraint specifies a unique boundary position.

This bistability, however, only happens when the initial domain size is sufficiently large. To demonstrate this, we repeat the simulations in Fig. 8 (where we start each profile at the uniform steady state at some places and zero in others), with a variety of initial domain sizes. We find that when the initial PAR-3 domain of enrichment is 50% of the domain or larger, the system tends to the bistable state, with about 85% of the domain enriched in PAR-3 and 15% at the lower state. When the initial domain of PAR-3 enrichment is too low, however, we find that the flux into the depleted regions is too large, and those regions tend to surpass the smaller uniform steady state and be attracted to the larger one. The higher flux happens because of a larger cytoplasmic concentration (which could result from the initial condition, or from unbinding from the enriched domain if we try to deplete the cytoplasm initially). In any case, the conclusion of Fig. 8 is that there is a uniform steady state, which is the attractor when most of the PAR-3 is initially in the cytoplasm, and a bistable state, which is an attractor when most of the PAR-3 is initially bound.

Let us now try to understand the position of the boundary. In Fig. 9, we plot the size of the enriched PAR-3 domain over time for various initial boundary positions. We recall that, without diffusion, the solution is given by (21). Thus, for sizes of the enriched PAR-3 domain larger than 0.6, the cytoplasmic concentration is sufficiently low that a bistable solution exists (left panel of

Fig. 9). When the PAR-3 domain is initially too small, the cytoplasmic concentration at steady state would be too high for bistability, and so the uniform state is the only stable one. If the bistable solution exists, then the boundary position does not move in time; any domain size greater than 0.6 appears to be stable.

This is not the case when we add diffusion into the model, which provides an additional constraint. Recall that the cytoplasm has to be sufficiently depleted for bistability to exist. Thus, without diffusion, the density of PAR-3 in the enriched zone grows when the boundary shrinks. But this increases the diffusive flux in the boundary layer between the enriched and depleted domains. The increased diffusive flux spreads the boundary back out. In the reverse case, when the boundary is too large, the binding rate plus diffusion in the boundary layer is not enough to compensate for the unbinding rate. The boundary then has to contract to enrich the cytoplasm more, and balance the two out. The unique boundary position occurs when the additional flux in the boundary layer from diffusion balances small differences in the binding and unbinding rates, as shown in the right panel of Fig. 9. The dimensionless feedback strength $\hat{K}_A^+$ gives some control over the intrinsic boundary – when $\hat{K}_A^+ = 12.5$, we obtain roughly 85% enriched PAR-3. When $\hat{K}_A^+ = 25$, we get roughly 90%, and when $\hat{K}_A^+ = 7$ we get about 75%. Of course we cannot make $\hat{K}_A^+$ too small, because then the uniform state becomes the only stable one.

Another way to think about diffusion in the boundary layer is the following: suppose that we set up the system at its steady state without diffusion. Then, when we turn on diffusion, there is diffusion of monomers away from the enrichment zone, and consequently local depletion of monomers at the edge of the enrichment zone (oligomers are not depleted, so the on flux is basically unchanged). There is then an imbalance of flux where the flux from binding is larger than the unbinding flux at the edge of the enrichment zone. If the on rate dominates diffusion (this is the case when the cytoplasm is enriched), then the boundary will tend to expand. On the other hand, if diffusive fluxes are sufficiently large (cytoplasmic depletion or larger zone of enrichment), then the boundary will contract if diffusive flux outwards overcomes the increased local binding. Figure 10 shows examples of this.
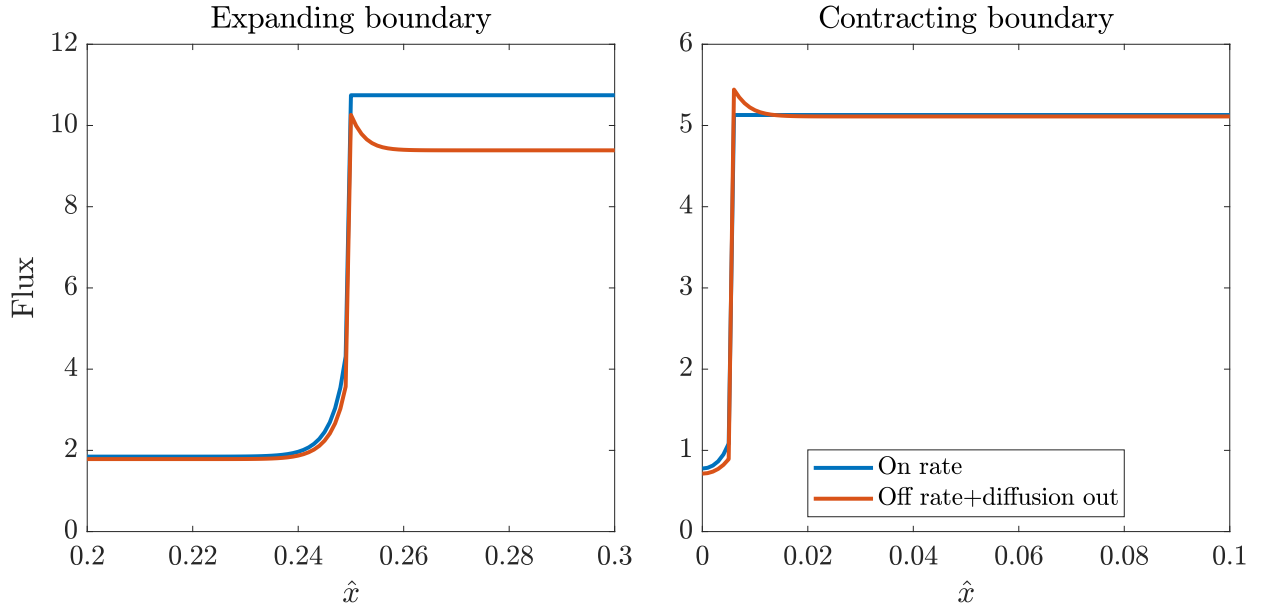
Figure 10: Local depletion by diffusion and consequent expansion/contraction of boundary. These figures show the positive fluxes due to binding (blue) and the negative fluxes due to diffusion and unbinding (red). When the boundary is narrow (left figure), the binding rate is higher due to enriched cytoplasm, and the boundary expands. On the other hand, when the boundary is wider (right figure), the binding rate is locally lower than the off rate + diffusion (note diffusion makes the difference in this case), and the boundary contracts.

2.3 PAR-3 / PAR-2 bistable model

Let's now add posterior PARs (PAR-2) to the model of PAR-3, so that the equations are

$$\partial_t A_1 = D_A \partial_x^2 A_1 + \left(k_A^{\mathrm{on}} + k_A^+ f_A^+ \left(A_1 + 2A_n \right) \right) A_{\mathrm{cyto}} - k_A^{\mathrm{off}} A_1 - 2k_A^{\mathrm{p}} A_1^2 + 2k_A^{\mathrm{dp}} A_n, \tag{22a}$$

$$\partial_t A_n = k_A^{\mathrm{p}} A_1^2 - k_A^{\mathrm{dp}} A_n - r_{\mathrm{PA}} A_n P \tag{22b}$$

$$\partial_t P = D_P \partial_x^2 P + k_P^{\mathrm{on}} P_{\mathrm{cyto}} - k_P^{\mathrm{off}} P - r_{\mathrm{AP}} P \left(A_1 + 2A_n \right), \tag{22c}$$

Here we have assumed that PAR-3 inhibits PAR-2 (by activating PKC-3, which is not included here for simplicity) [9]. It is possible here to model PAR-2 in terms of both dimers and monomers [1]; however, because PKC-3 acts on both monomers and dimers, the two are really only separated by kinetics of dimerization. Furthermore, a single species model of PAR-2 has already been made in [5], and the parameters for such a model were already fit there. As such, we will use a single species model for PAR-2.

Repeating our non-dimensionalization from (18), the dimensionless form of the equations (22) is

$$\partial_{\hat{t}} \hat{A}_1 = \hat{D}_A \partial_{\hat{x}}^2 A_1 + \hat{K}_A^{\mathrm{on}} \left(1 + \hat{K}_A^+ f_A^+ \left(\hat{A}_1 + 2\hat{A}_n \right) \right) \left(1 - \int_0^1 \left(\hat{A}_1(x) + 2\hat{A}_n(x) \right) d\hat{x} \right)$$
$$+ 2\hat{K}_A^{\mathrm{dp}} \hat{A}_n - 2\hat{K}_A^{\mathrm{p}} \hat{A}_1^{\,2} - \hat{K}_A^{\mathrm{off}} \hat{A}_1 \tag{23a}$$

$$\partial_{\hat{t}} \hat{A}_n = \hat{K}_A^{\mathrm{p}} \hat{A}_1^{\,2} - \hat{K}_A^{\mathrm{dp}} \hat{A}_n - \frac{r_{\mathrm{PA}} P^{(\mathrm{Tot})}}{k_A^{\mathrm{dp}}} \hat{P} \hat{A}_n \tag{23b}$$

$$\partial_{\hat{t}} \hat{P} = \hat{D}_P \partial_{\hat{x}}^2 \hat{P} + \hat{K}_P^{\mathrm{on}} \left(1 - \int_0^1 \hat{P}(\hat{x}) \, d\hat{x} \right) - \hat{K}_P^{\mathrm{off}} \hat{P} - \frac{r_{\mathrm{AP}} A^{(\mathrm{Tot})}}{k_A^{\mathrm{dp}}} \left(\hat{A}_1 + 2\hat{A}_n \right) \hat{P} \tag{23c}$$

$$\hat{D}_A = \frac{D_A}{L^2 k_A^{\mathrm{dp}}}, \quad \hat{K}_A^{\mathrm{on}} = \frac{k_A^{\mathrm{on}}}{k_A^{\mathrm{dp}} h}, \quad \hat{K}_A^+ = \frac{k_A^+}{k_A^{\mathrm{on}}}, \quad \hat{K}_A^{\mathrm{off}} = \frac{k_A^{\mathrm{off}}}{k_A^{\mathrm{dp}}}, \quad \hat{K}_A^{\mathrm{p}} = \frac{k_A^{\mathrm{p}} A^{(\mathrm{Tot})}}{k_A^{\mathrm{dp}}}, \quad \hat{K}_A^{\mathrm{dp}} = 1 \tag{23d}$$

$$\hat{D}_P = \frac{D_P}{L^2 k_A^{\mathrm{dp}}} \quad \hat{K}_P^{\mathrm{on}} = \frac{k_P^{\mathrm{on}}}{k_A^{\mathrm{dp}} h}, \quad \hat{K}_P^{\mathrm{off}} = \frac{k_P^{\mathrm{off}}}{k_A^{\mathrm{dp}}} \tag{23e}$$

Using the parameters in Table 2, there are three unknown parameters here: the feedback strength K_A^+, which we will fix at $K_A^+ = 12.5$ to obtain bistability of the intrinsic PAR-3 dynamics, and the inhibition parameters r_{AP} and r_{PA}. For simplicity, we will assume $r_{\mathrm{AP}} = r_{\mathrm{PA}}$.

As an illustration of how this model behaves, in Figs. 11 and 12 we examine how initial zones of mutually excluded PAR-3 and PAR-2 enrichment evolve to steady state. The key here is the dynamics of PAR-3, which we recall switches between a small steady state (typically associated with the posterior half), and a larger steady state (typically associated with the anterior half). When there is no inhibition, PAR-3 develops its bistable state naturally, and PAR-2 is spread uniformly.
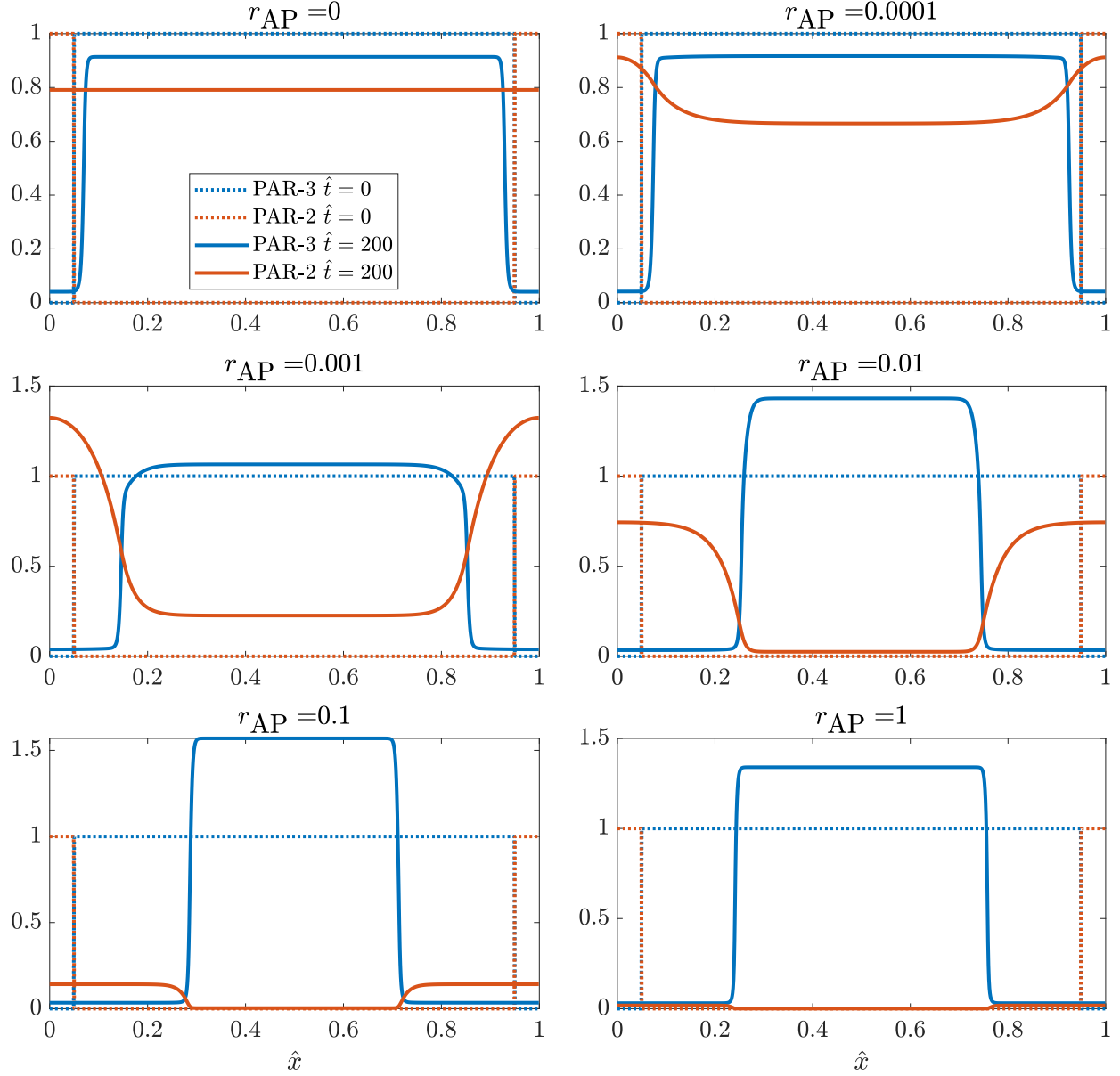
Figure 11: Dynamics of the PAR-2/PAR-3 model (23) with an initial small zone of PAR-2 enrichment and PAR-3 depletion. The dotted lines show the initial conditions (90% PAR-3 enrichment), while the solid lines show the steady state, both for PAR-3 in blue and PAR-2 in red.
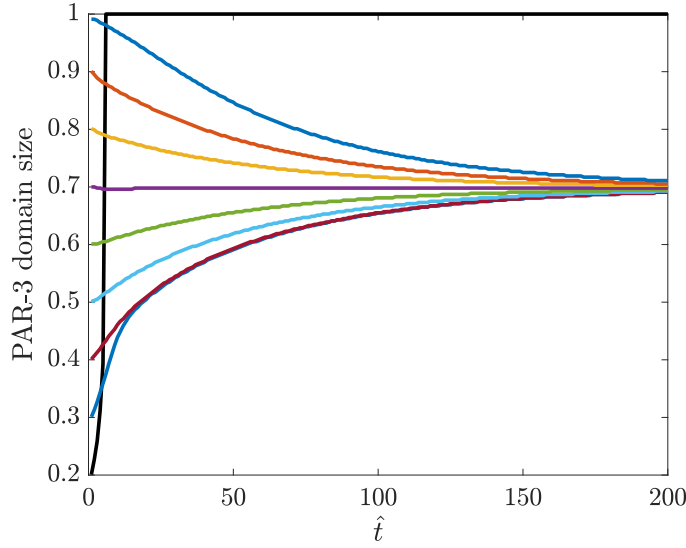
Figure 12: Size of the PAR-3 enrichment zone over time. Simulations use $r_{AP} = 10^{-3}$ and start with PAR-3 at its uniform steady state value in an enrichment zone (e.g., the simulations in Fig. 11 start at 0.9). We then watch the size of the domain evolve over time. If there is sufficient cytoplasmic depletion of PAR-3, then mutual inhibition by PAR-2 shifts the intrinsic boundary.

Increasing the mutual inhibition then causes the boundary to shift, as depletion of PAR-2 in the interior leads to more cytoplasmic PAR-2, which increases the on rate in the inhibited zone. The attaching PAR-2 then diffuses, out-competing the PAR-3 and driving it to a lower steady state. This shifts the boundary. When mutual inhibition goes back up, PAR-2 simply can't do anything because the mutual inhibition is too strong. We note also the shape of the peak in PAR-2 is more broad than for PAR-3, since we assume that PAR-2 can diffuse in the membrane with a higher diffusion coefficient than even monomeric PAR-3, and since PAR-3 is mostly in the non-diffusive oligomer form.

2.3.1 Parameters encode a unique boundary position

We now zero in on one particular parameter set to demonstrate that the steady state boundary position is set uniquely by the parameters. When $r_{AP} = 10^{-3}$, Fig. 11 shows that the domain of PAR-3 enrichment at steady state is roughly 70%. We confirm that this is a unique steady state in Fig. 12 by changing length of the region initially enriched in PAR-3. We find that, as long as the domain size is larger than 0.2, we see a unique steady state where PAR-3 and PAR-2 mutually exclude each other. By contrast, when the initial domain of enrichment is too small,

there is sufficient cytoplasmic PAR-3 for the uniform steady state to be the only stable one. These dynamics are similar to the case of PAR-3 alone (Fig. 9), except that PAR-2 shifts the boundary by driving PAR-3 down to the smaller steady state in some regions.

2.3.2   Finding the inhibition strength r_{AP}

We have two main experimental observations to constrain the inhibition strength r_{AP}:

1. In embryos depleted of myosin (whether wild-type or ECT-2 (RNAi)), the PAR-3 domain takes up about 75% of the embryo [16, Fig. 5B].

2. In wild-type embryos, the level of PAR-3 at the posterior is roughly 2% of the anterior level [13, Fig. 4C].

In the case when $r_{\mathrm{AP}} = 6 \times 10^{-4}$, we obtain a PAR-3 domain which takes up 75% of the embryo and a ratio of $0.04/1.03 \approx 0.04$. This falls roughly within the experimental parameter range, and so this is the parameter we will use going forward.

2.4   Model of PAR-2 and PAR-3 with myosin

Let's now add myosin to the model of PAR-2 and PAR-3 that we formulated in (23). Myosin enters here as an advective flow for each of the proteins, then has its own constitutive equation. The full

dimensionless model is given by

$$\partial_{\hat{t}}\hat{A}_1 + \hat{\sigma}_0\partial_{\hat{x}}\left(\hat{v}\hat{A}_1\right) = \hat{D}_A\partial_{\hat{x}}^2\hat{A}_1 + \hat{K}_A^{\mathrm{on}}\left(1 + \hat{K}_A^+ f_A^+\left(\hat{A}_1(x) + 2\hat{A}_n(x)\right)\right)\left(1 - \int_0^1\left(\hat{A}_1(x) + 2\hat{A}_n(x)\right)d\hat{x}\right)$$
$$-\hat{K}_A^{\mathrm{off}}\hat{A}_1 + 2\hat{K}_A^{\mathrm{dp}}\hat{A}_n - 2\hat{K}_A^{\mathrm{p}}\hat{A}_1^2 \tag{24a}$$

$$\partial_{\hat{t}}\hat{A}_n + \hat{\sigma}_0\partial_{\hat{x}}\left(\hat{v}\hat{A}_n\right) = \hat{K}_A^{\mathrm{p}}\hat{A}_1^{\,2} - \hat{K}_A^{\mathrm{dp}}\hat{A}_n - \frac{r_{\mathrm{PA}}P^{(\mathrm{Tot})}}{k_A^{\mathrm{dp}}}\hat{P}\hat{A}_n \tag{24b}$$

$$\partial_{\hat{t}}\hat{P} + \hat{\sigma}_0\partial_{\hat{x}}\left(\hat{v}\hat{P}\right) = \hat{D}_P\partial_{\hat{x}}^2\hat{P} + \hat{K}_P^{\mathrm{on}}\left(1 - \int_0^1\hat{P}(\hat{x})\,d\hat{x}\right) - \hat{K}_P^{\mathrm{off}}\hat{P} - \frac{r_{\mathrm{AP}}A^{(\mathrm{Tot})}}{k_A^{\mathrm{dp}}}\left(\hat{A}_1 + 2\hat{A}_n\right)\hat{P} \tag{24c}$$

$$\partial_{\hat{t}}\hat{M} + \hat{\sigma}_0\partial_{\hat{x}}\left(\hat{v}\hat{M}\right) = \hat{D}_M\partial_{\hat{x}}^2\hat{M} + \hat{K}_M^{\mathrm{on}}\left(1 - \int_0^1\hat{M}(x)\,dx\right) - \left(\hat{K}_M^{\mathrm{off}} + \frac{r_{\mathrm{PM}}P^{(\mathrm{Tot})}}{k_A^{\mathrm{dp}}}\hat{P}\right)\hat{M} \tag{24d}$$

$$\hat{v} = \hat{\ell}^2\partial_{\hat{x}}^2 v + \hat{\ell}\partial_{\hat{x}}\hat{\sigma}_a(\hat{M}) \tag{24e}$$

$$\hat{D}_A = \frac{D_A}{L^2 k_A^{\mathrm{dp}}}, \quad \hat{K}_A^{\mathrm{on}} = \frac{k_A^{\mathrm{on}}}{k_A^{\mathrm{dp}}h}, \hat{K}_A^{\mathrm{off}} = \frac{k_A^{\mathrm{off}}}{k_A^{\mathrm{dp}}}, \quad \hat{K}_A^{\mathrm{dp}} = 1, \quad \hat{K}_A^{\mathrm{p}} = \frac{k_A^{\mathrm{p}}A^{(\mathrm{Tot})}}{k_A^{\mathrm{dp}}}, \quad \hat{K}_A^+ = \frac{k_A^+}{k_A^{\mathrm{on}}}$$

$$\hat{D}_P = \frac{D_P}{L^2 k_A^{\mathrm{dp}}}, \quad \hat{K}_P^{\mathrm{on}} = \frac{k_P^{\mathrm{on}}}{k_A^{\mathrm{dp}}h}, \quad \hat{K}_P^{\mathrm{off}} = \frac{k_P^{\mathrm{off}}}{k_A^{\mathrm{dp}}}, \quad \hat{\sigma}_0 = \left(\frac{\sigma_0/\sqrt{\eta\gamma}}{Lk_A^{\mathrm{dp}}}\right) \tag{24f}$$

$$\hat{D}_M = \frac{D_M}{k_A^{\mathrm{dp}}L^2}, \quad \hat{K}_M^{\mathrm{on}} = \frac{k_M^{\mathrm{on}}}{hk_A^{\mathrm{dp}}}, \quad \hat{K}_M^{\mathrm{off}} = \frac{k_M^{\mathrm{off}}}{k_A^{\mathrm{dp}}}, \quad \hat{\ell} = \frac{\sqrt{\eta/\gamma}}{L} \quad v = \hat{v}\frac{\sigma_0}{\sqrt{\eta\gamma}}.$$

Our key assumption here is that the posterior PAR-2 inhibits myosin activity through the reaction coefficient r_{PM} (units μm/s). Recalling our previous study of PAR-2 and PAR-3 in Section 2.3, we saw there that for strong enough mutual inhibition of the two proteins, the intrinsic bistability of PAR-3 can combine with mutual inhibition of PAR-2 to set up two mutually exclusive domains of enriched PAR-2 and PAR-3 (respectively).

But can we use myosin as a means to shift the boundary? Figure 13 shows that indeed we can. Here we consider the same parameters as given in Table 2, but add myosin with the parameters given in Table 1. In order to get more bound myosin, we increase to $k_M^{\mathrm{on}} = 2$ μm/s (a factor of 10 relative to the value reported in [5], which is based on fitting a different model). The dotted lines in each plot show the steady state with $r_{\mathrm{PM}} = 0$, so that we can see how adding PAR-2 inhibition of myosin shifts the boundary. Starting with $r_{\mathrm{PM}} = 10^{-4}$ up to $r_{\mathrm{PM}} = 0.1$, we see a PAR-3 domain which shrinks with increasing r_{PM}, until the inhibition is so high that no flow is generated at all.

What stops the boundary from expanding? The boundary between the domains expands when there is enough flow of PAR-2 so as to push PAR-3 from its higher steady state to its lower one. The flow of PAR-2 is linked to the gradient in myosin, which in turn depends on the gradient of PAR-2. The amount of PAR-2 comes from cytoplasm. The flow is therefore: cytoplasmic PAR-2 depleted $\to$ PAR-2 cannot increase anymore $\to$ no myosin inhibition $\to$ boundary stops moving. In
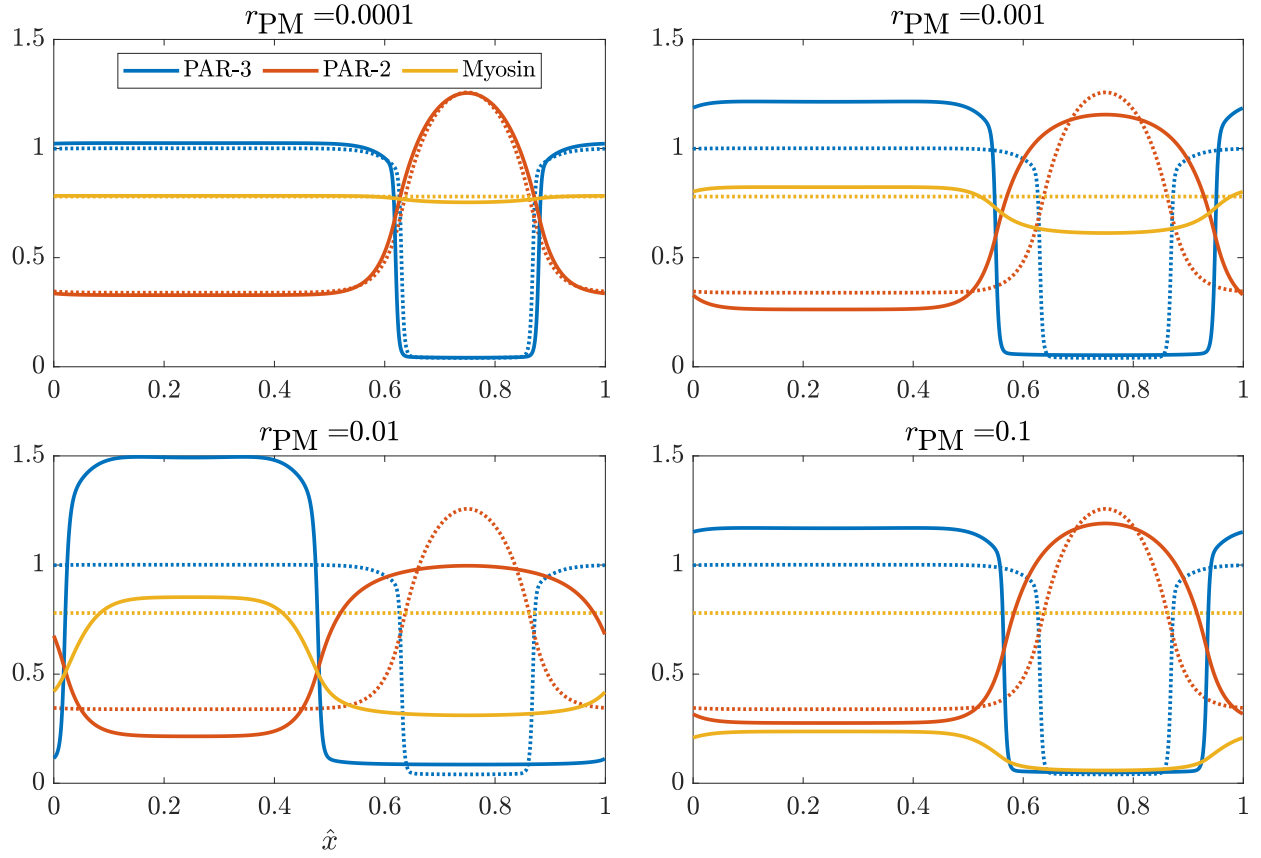
Figure 13: Fixing $r_{AP} = 6 \times 10^{-4}$ and changing the degree to which PAR-2 inhibits myosin in the model (24). The dotted lines show the steady state when $r_{PM} = 0$ (blue for PAR-3, red for PAR-2, yellow for myosin), while the solid lines show the steady state with the value of r_{PM} indicated in the title.

Parameter	Description	Value	Units	Ref	Notes
D_C	CDC-42 diffusivity	0.1	$\mu\text{m}^2/\text{s}$	[12]	
k_C^{on}	CDC-42/PAR-6 attachment rate	0.02	$\mu\text{m}/\text{s}$	[5]	
k_C^{off}	PAR-6/CDC-42 detachment rate	0.01	$1/\text{s}$	[12]	
$C^{(\text{Tot})}$	Maximum bound CDC-42 density	1500	$\#/\mu\text{m}$	[5]	Same for all PARs

Table 3: Parameter values for new species C.

the case when there is unlimited cytoplasmic PAR-2, the limit then becomes cytoplasmic PAR-3. The on rate keeps getting higher as we deplete PAR-3, until it outcompetes everything.

2.5 Comparison with experiments

We now attempt an honest comparison with the experimental data. Section 2.3.2 already discussed how we found r_{AP} (aPAR/pPAR inhibition strength), which leaves one unknown parameter: the inhibition of myosin by pPARs r_{PM}. We choose it so that the myosin boundary is at roughly 50% of the embryo, thus setting $r_{\text{PM}} = 0.005$.

Figure 14 provides a comparison between the model and experimental data in NMY-2::GFP embryos (we are tracking myosin in fluorescence microscopy). The top plot shows the myosin intensity profile, comparing wild-type (black), branched actin knockdown via *arx-2* (RNAi) (pink), and the model (red). The intensity profile in the *arx-2* (RNAi) embryos compares favorably with the model; as there is a zone of low intensity in the posterior half and transitioning to zone of high intensity at the anterior half.

3 CDC-42 as the master regulator of myosin and branched actin

Our model in the previous section demonstrates that we can account for the behavior *without* branched actin with a simple three species model of PAR-3, posterior PARs (PAR-2 specifically, but P stands for all of them), and myosin. With branched actin, our model has to change to account for the stalling contractility and decrease in myosin concentration at the anterior pole. We do this by introducing a new species, called C, which represents the "other" aPARs, in particular CDC-42. Once we have access to the profile of CDC-42, we will be able to test different assumptions about myosin and branched actin.
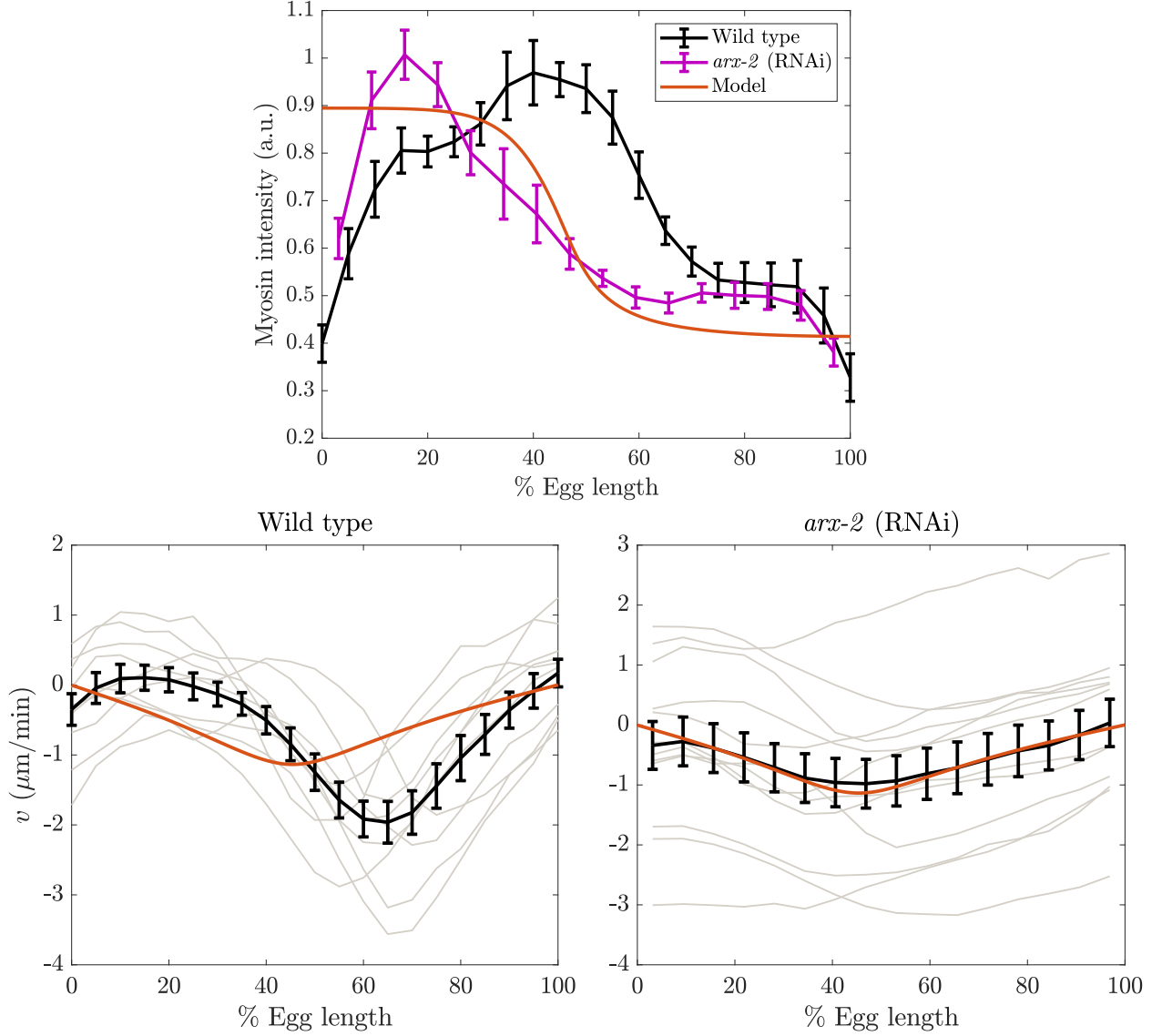
Figure 14: Comparing myosin intensity (top) and flow fields (bottom) from experiments to the model (24) at steady state $(\hat{t} = 200)$. The parameters $r_{\mathrm{AP}} = 0.0006$ μm/s and $r_{\mathrm{PM}} = 0.005$ μm/s are chosen so that the A/P boundary is at 70% of the egg length without myosin and roughly 45% of the egg length with myosin. In all cases, we compare wild-type embryos (black) and *arx-2* (RNAi) embryos (pink) with the model (red). In the flow profiles, the gray lines show individual embryos, while the black lines show the mean (error bars are one standard error in the mean).
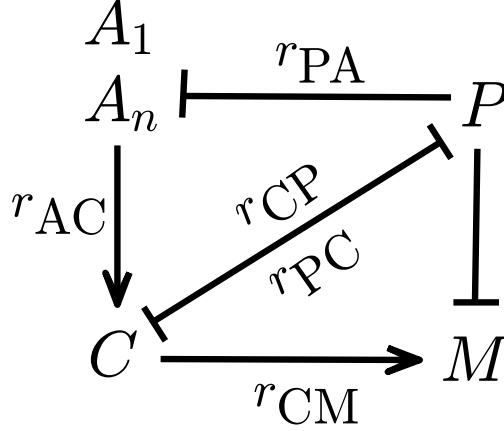
Figure 15: Model schematic for this section. A_1 and A_n represent PAR-3 monomers and oligomers. P represents pPARs, C represents aPARs other than PAR-3, and M represents myosin.

3.1 Biochemistry without contractility

As in the previous section, let's start by just considering the biochemistry without myosin. We introduce a variable C to represent CDC-42, and generally any anterior PAR proteins that are not PAR-3. Adding this to the previous biochemistry model (22) gives

$$\partial_t A_1 = D_A \partial_x^2 A_1 + \left(k_A^{\text{on}} + k_A^+ f_A^+ \left(A_1 + 2A_n\right)\right) A_{\text{cyto}} - k_A^{\text{off}} A_1 - 2k_A^{\text{p}} A_1^2 + 2k_A^{\text{dp}} A_n, \tag{25a}$$

$$\partial_t A_n = k_A^{\text{p}} A_1^2 - k_A^{\text{dp}} A_n - r_{\text{PA}} A_n P \tag{25b}$$

$$\partial_t C = D_C \partial_x^2 C + \left(k_C^{\text{on}} + r_{\text{AC}} A\right) C_{\text{cyto}} - k_C^{\text{off}} C - r_{\text{PC}} C P \tag{25c}$$

$$\partial_t P = D_P \partial_x^2 P + k_P^{\text{on}} P_{\text{cyto}} - k_P^{\text{off}} P - r_{\text{CP}} P C, \tag{25d}$$

Comparing to the model (25), we have slightly reworked the biochemistry. Instead of inhibiting PAR-2 directly, PAR-3 now inhibits PAR-2 by promoting the diffusable aPAR C, which directly inhibits PAR-2. This should not really change the fundamental model behavior. A summary diagram is shown in Fig. 15, where for this section we are not considering any interactions with myosin M.

Repeating our non-dimensionalization from (23), the dimensionless form of the equations (25)

31

is

$$\partial_{\hat{t}}\hat{A}_1 = \hat{D}_A\partial_{\hat{x}}^2 A_1 + \hat{K}_A^{\text{on}}\left(1 + \hat{K}_A^+ f_A^+\left(\hat{A}_1 + 2\hat{A}_n\right)\right)\left(1 - \int_0^1\left(\hat{A}_1(x) + 2\hat{A}_n(x)\right)d\hat{x}\right)$$
$$+ 2\hat{K}_A^{\text{dp}}\hat{A}_n - 2\hat{K}_A^{\text{p}}\hat{A}_1^2 - \hat{K}_A^{\text{off}}\hat{A}_1 \tag{26a}$$

$$\partial_{\hat{t}}\hat{A}_n = \hat{K}_A^{\text{p}}\hat{A}_1^2 - \hat{K}_A^{\text{dp}}\hat{A}_n - \frac{r_{\text{PA}}P^{(\text{Tot})}}{k_A^{\text{dp}}}\hat{P}\hat{A}_n \tag{26b}$$

$$\partial_{\hat{t}}\hat{C} = \hat{D}_C\partial_{\hat{x}}^2\hat{P} + \hat{K}_C^{\text{on}}\left(1 + \hat{R}_{\text{AC}}\left(\hat{A}_1 + 2\hat{A}_n\right)\right)\left(1 - \int_0^1\hat{C}(\hat{x})\,d\hat{x}\right) - \hat{K}_C^{\text{off}}\hat{C} - \frac{r_{\text{PC}}P^{(\text{Tot})}}{k_A^{\text{dp}}}\hat{P}\hat{C} \tag{26c}$$

$$\partial_{\hat{t}}\hat{P} = \hat{D}_P\partial_{\hat{x}}^2\hat{P} + \hat{K}_P^{\text{on}}\left(1 - \int_0^1\hat{P}(\hat{x})\,d\hat{x}\right) - \hat{K}_P^{\text{off}}\hat{P} - \frac{r_{\text{CP}}C^{(\text{Tot})}}{k_A^{\text{dp}}}\hat{C}\hat{P} \tag{26d}$$

$$\hat{D}_A = \frac{D_A}{L^2 k_A^{\text{dp}}}, \quad \hat{K}_A^{\text{on}} = \frac{k_A^{\text{on}}}{k_A^{\text{dp}}h}, \quad \hat{K}_A^+ = \frac{k_A^+}{k_A^{\text{on}}}, \quad \hat{K}_A^{\text{off}} = \frac{k_A^{\text{off}}}{k_A^{\text{dp}}}, \quad \hat{K}_A^{\text{p}} = \frac{k_A^{\text{p}}A^{(\text{Tot})}}{k_A^{\text{dp}}}, \quad \hat{K}_A^{\text{dp}} = 1 \tag{26e}$$

$$\hat{D}_P = \frac{D_P}{L^2 k_A^{\text{dp}}} \quad \hat{K}_P^{\text{on}} = \frac{k_P^{\text{on}}}{k_A^{\text{dp}}h}, \quad \hat{K}_P^{\text{off}} = \frac{k_P^{\text{off}}}{k_A^{\text{dp}}} \tag{26f}$$

$$\hat{D}_C = \frac{D_C}{L^2 k_A^{\text{dp}}} \quad \hat{K}_C^{\text{on}} = \frac{k_C^{\text{on}}}{k_A^{\text{dp}}h}, \quad \hat{K}_C^{\text{off}} = \frac{k_C^{\text{off}}}{k_A^{\text{dp}}}, \quad \hat{R}_{\text{AC}} = \frac{r_{\text{AC}}A^{(\text{Tot})}}{k_C^{\text{on}}} \tag{26g}$$

Using the parameters in Tables 1 and 2, there are four unknown parameters here: r_{PA} (inhibition of PAR-3 by pPARs), r_{PC} and r_{CP} (mutual inhibition of pPARs and aPARs), and r_{AC} (rate at which PAR-3 promotes CDC-42). We estimate them in the next section; Table 4 provides a summary for convenience.

3.1.1 Estimating the unknown parameters

The first unknown parameter is r_{PC}, which is the inhibition of C (which stands for CDC-42, PAR-6, and PKC-3) by P (which stands for all the pPARs). To estimate this parameter, we solve (26c) at steady state in the absence of A to obtain

$$\hat{C} = \frac{1}{1 + \frac{hk_c^{\text{off}}}{k_C^{\text{on}}} + \frac{r_{\text{CP}}h}{k_C^{\text{on}}}P^{(\text{Tot})}\hat{P}}. \tag{27}$$

Now according to [13], in a system of units where $\hat{C} = 1$ when $\hat{P} = 0$, we have $\hat{C} \approx 1/(1 + 13.3\hat{P})$, which implies that

$$13.3 = \frac{r_{\text{CP}}hP^{(\text{Tot})}}{k_C^{\text{on}} + hk_C^{\text{off}}} \rightarrow r_{\text{CP}} = 3.8 \times 10^{-3}\,\mu\text{m/s}.$$

So we have found the inhibition of C by P. Because inhibition of P by C is fundamentally the same loop, we will assume $r_{\text{PC}} = r_{\text{CP}}$. This sets two of the parameters.

Our next observation from [13] is that for PAR-1 mutant embryos, the amount of PAR-6 in the posterior is 20–25% of the anterior. PAR-1 mutants are important in our new circuit because they

| Parameter	Description	Value	Units	Ref	Notes
r_{PC}	P inhibiting C	3.8×10^{-3}	μm/s	[13]	Fitting CDC/CHIN-1 relationship (Fig. A5)
r_{CP}	C inhibiting P	3.8×10^{-3}	μm/s	[13]	Same as r_{PC}
r_{AC}	A promoting C	8×10^{-4}	μm^2/s	[13]	20–25% anterior C when $r_{PA} = 0$
r_{AP}	P inhibiting A	6×10^{-4}	μm/s	[16]	75% A enrichment no myosin

Table 4: Values for unknown reaction parameters in the models of this section.
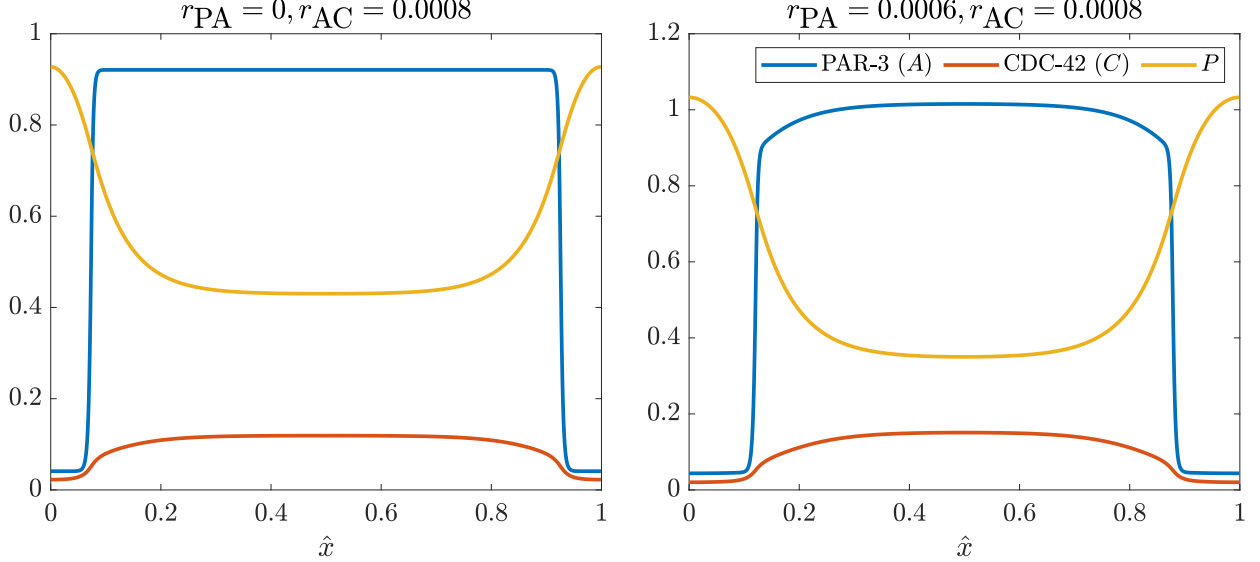
Figure 16: Steady states in the model (26). We fix the parameter $r_{PC} = r_{CP} = 3.8 \times 10^{-3} \, \mu$m/s, which leaves two unknown parameters. At left, we set $r_{PA} = 0$, so that there is no inhibition of A by P. This means that asymmetries in C are driven by A only, which allows us to set r_{AC} to match experimental observations. At right, we then introduce inhibition of A by P and fit the boundary position.

remove the inhibition of PAR-3 by pPARs, so that $r_{AP} = 0$. Thus, when $r_{AP} = 0$, we want to choose r_{AC} (promotion of C by A) to match the experimental observation. Figure 16 shows our attempt to do this. In the left panel, we tune r_{AC} so that the C (PAR-6/CDC-42/PKC-3) concentration is about 25% in the posterior regions to its value in the anterior regions. In the right panel, we then introduce $r_{PA} = 6 \times 10^{-4} \, \mu$m/s (determined in Section 2.3.2) and see how the boundary position changes from our earlier parameters. Previously, we saw that this value of r_{PA} gave a boundary position at roughly 75% of the embryo length. The right panel of Fig. 16 establishes that this is still the case.

To be more precise about the position of the boundary under these parameters, in Fig. 17 we repeat our experiment of starting with some percentage of the domain enriched in PAR-3, then
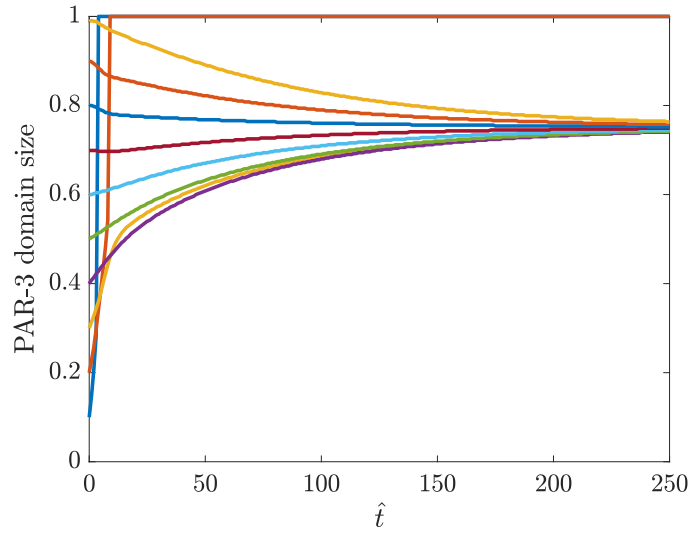
Figure 17: Boundary position in the model (26) starting from different initial conditions. We locally enrich PAR-3 and C, then plot the size of the enriched domain over time. There is a unique steady state which sits around 75% embryo length.

watching the evolution to steady state. As in the previous section, we once again see bistable dynamics where the PAR-3 boundary can...

3.2 Incorporating myosin

$$\partial_{\hat{t}}\hat{A}_1 + \hat{\sigma}_0\partial_{\hat{x}}\left(\hat{v}\hat{A}_1\right) = \hat{D}_A\partial_{\hat{x}}^2\hat{A}_1 + \hat{K}_A^{\text{on}}\left(1 + \hat{K}_A^+ f_A^+\left(\hat{A}_1(x) + 2\hat{A}_n(x)\right)\right)\left(1 - \int_0^1\left(\hat{A}_1(x) + 2\hat{A}_n(x)\right)d\hat{x}\right)$$

$$- \hat{K}_A^{\text{off}}\hat{A}_1 + 2\hat{K}_A^{\text{dp}}\hat{A}_n - 2\hat{K}_A^{\text{p}}\hat{A}_1^2 \tag{28a}$$

$$\partial_{\hat{t}}\hat{A}_n + \hat{\sigma}_0\partial_{\hat{x}}\left(\hat{v}\hat{A}_n\right) = \hat{K}_A^{\text{p}}\hat{A}_1^{\,2} - \hat{K}_A^{\text{dp}}\hat{A}_n - \frac{r_{\text{PA}}P^{(\text{Tot})}}{k_A^{\text{dp}}}\hat{P}\hat{A}_n \tag{28b}$$

$$\partial_{\hat{t}}\hat{P} + \hat{\sigma}_0\partial_{\hat{x}}\left(\hat{v}\hat{P}\right) = \hat{D}_P\partial_{\hat{x}}^2\hat{P} + \hat{K}_P^{\text{on}}\left(1 - \int_0^1\hat{P}(\hat{x})\,d\hat{x}\right) - \hat{K}_P^{\text{off}}\hat{P} - \frac{r_{\text{CP}}C^{(\text{Tot})}}{k_A^{\text{dp}}}\hat{C}\hat{P} \tag{28c}$$

$$\partial_{\hat{t}}\hat{C} + \hat{\sigma}_0\partial_{\hat{x}}\left(\hat{v}\hat{C}\right) = \hat{D}_C\partial_{\hat{x}}^2\hat{P} + \hat{K}_C^{\text{on}}\left(1 + \hat{R}_{\text{AC}}\left(\hat{A}_1 + 2\hat{A}_n\right)\right)\left(1 - \int_0^1\hat{C}(\hat{x})\,d\hat{x}\right)$$

$$- \hat{K}_C^{\text{off}}\hat{C} - \frac{r_{\text{PC}}P^{(\text{Tot})}}{k_A^{\text{dp}}}\hat{P}\hat{C} \tag{28d}$$

$$\partial_{\hat{t}}\hat{M} + \hat{\sigma}_0\partial_{\hat{x}}\left(\hat{v}\hat{M}\right) = \hat{D}_M\partial_{\hat{x}}^2\hat{M} + \hat{K}_M^{\text{on}}\left(1 + \hat{R}_{\text{CM}}\hat{C}\right)\left(1 - \int_0^1\hat{M}(x)\,dx\right)$$

$$- \left(\hat{K}_M^{\text{off}} + \frac{r_{\text{PM}}P^{(\text{Tot})}}{k_A^{\text{dp}}}\hat{P}\right)\hat{M} \tag{28e}$$

$$\hat{v} = \hat{\ell}^2\partial_{\hat{x}}^2 v + \hat{\ell}\partial_{\hat{x}}\hat{\sigma}_a(\hat{M}) \tag{28f}$$

$$\hat{D}_A = \frac{D_A}{L^2 k_A^{\text{dp}}}, \quad \hat{K}_A^{\text{on}} = \frac{k_A^{\text{on}}}{k_A^{\text{dp}}h}, \hat{K}_A^{\text{off}} = \frac{k_A^{\text{off}}}{k_A^{\text{dp}}}, \quad \hat{K}_A^{\text{dp}} = 1, \quad \hat{K}_A^{\text{p}} = \frac{k_A^{\text{p}}A^{(\text{Tot})}}{k_A^{\text{dp}}}, \quad \hat{K}_A^+ = \frac{k_A^+}{k_A^{\text{on}}}$$

$$\hat{D}_P = \frac{D_P}{L^2 k_A^{\text{dp}}}, \quad \hat{K}_P^{\text{on}} = \frac{k_P^{\text{on}}}{k_A^{\text{dp}}h}, \quad \hat{K}_P^{\text{off}} = \frac{k_P^{\text{off}}}{k_A^{\text{dp}}}, \quad \hat{\sigma}_0 = \left(\frac{\sigma_0/\sqrt{\eta\gamma}}{Lk_A^{\text{dp}}}\right) \tag{28g}$$

$$\hat{D}_M = \frac{D_M}{k_A^{\text{dp}}L^2}, \quad \hat{K}_M^{\text{on}} = \frac{k_M^{\text{on}}}{hk_A^{\text{dp}}}, \quad \hat{K}_M^{\text{off}} = \frac{k_M^{\text{off}}}{k_A^{\text{dp}}}, \quad \hat{\ell} = \frac{\sqrt{\eta/\gamma}}{L} \quad v = \hat{v}\frac{\sigma_0}{\sqrt{\eta\gamma}}, \quad \hat{R}_{\text{CM}} = \frac{r_{\text{CM}}C^{(\text{Tot})}}{k_M^{\text{on}}}$$

$$\hat{D}_C = \frac{D_C}{L^2 k_A^{\text{dp}}} \quad \hat{K}_C^{\text{on}} = \frac{k_C^{\text{on}}}{k_A^{\text{dp}}h}, \quad \hat{K}_C^{\text{off}} = \frac{k_C^{\text{off}}}{k_A^{\text{dp}}}, \quad \hat{R}_{\text{AC}} = \frac{r_{\text{AC}}A^{(\text{Tot})}}{k_C^{\text{on}}}$$

References

[1] Tom Bland, Nisha Hirani, David Briggs, Riccardo Rossetto, KangBo Ng, Neil Q McDonald, David Zwicker, and Nathan W Goehring. Optimized dimerization of the par-2 ring domain drives cooperative and selective membrane recruitment for robust feedback-driven cell polarization. *bioRxiv*, pages 2023–08, 2023.

[2] Justin S Bois, Frank Jülicher, and Stephan W Grill. Pattern formation in active fluids. *Biophysical Journal*, 100(3):445a, 2011.

[3] Adriana T Dawes and Edwin M Munro. Par-3 oligomerization may provide an actin-independent mechanism to maintain distinct par protein domains in the early caenorhabditis elegans embryo. *Biophysical journal*, 101(6):1412–1422, 2011.

[4] Nathan W Goehring, Philipp Khuc Trong, Justin S Bois, Debanjan Chowdhury, Ernesto M Nicola, Anthony A Hyman, and Stephan W Grill. Polarization of par proteins by advective triggering of a pattern-forming system. *Science*, 334(6059):1137–1141, 2011.

[5] Peter Gross, K Vijay Kumar, Nathan W Goehring, Justin S Bois, Carsten Hoege, Frank Jülicher, and Stephan W Grill. Guiding self-organized pattern formation in cell polarity establishment. *Nature physics*, 15(3):293–300, 2019.

[6] Jacob Halatek, Fridtjof Brauns, and Erwin Frey. Self-organization principles of intracellular pattern formation. *Philosophical Transactions of the Royal Society B: Biological Sciences*, 373(1747):20170107, 2018.

[7] Rukshala Illukkumbura, Nisha Hirani, Joana Borrego-Pinto, Tom Bland, KangBo Ng, Lars Hubatsch, Jessica McQuade, Robert G Endres, and Nathan W Goehring. Design principles for selective polarization of par proteins by cortical flows. *Journal of Cell Biology*, 222(8), 2023.

[8] Charles F Lang, Alexander Anneken, and Edwin Munro. Oligomerization and feedback on membrane recruitment stabilize par-3 asymmetries in c. elegans zygotes. *bioRxiv*, pages 2023–08, 2023.

[9] Charles F Lang and Edwin Munro. The par proteins: from molecular circuits to dynamic self-stabilizing cell polarity. *Development*, 144(19):3405–3416, 2017.

[10] Charles F Lang and Edwin M Munro. Oligomerization of peripheral membrane proteins provides tunable control of cell surface polarity. *Biophysical Journal*, 121(23):4543–4559, 2022.

[11] Alex Mogilner, Jun Allard, and Roy Wollman. Cell polarity: quantitative modeling as a tool in cell biology. *Science*, 336(6078):175–179, 2012.

[12] François B Robin, William M McFadden, Baixue Yao, and Edwin M Munro. Single-molecule analysis of cell surface dynamics in caenorhabditis elegans embryos. *Nature methods*, 11(6):677–682, 2014.

[13] Anne Sailer, Alexander Anneken, Younan Li, Sam Lee, and Edwin Munro. Dynamic opposition of clustered proteins stabilizes cortical polarity in the c. elegans zygote. *Developmental cell*, 35(1):131–142, 2015.

[14] Filipe Tostevin and Martin Howard. Modeling the establishment of par protein polarity in the one-cell c. elegans embryo. *Biophysical journal*, 95(10):4512–4522, 2008.

[15] Philipp Khuc Trong, Ernesto M Nicola, Nathan W Goehring, K Vijay Kumar, and Stephan W Grill. Parameter-space topology of models for cell polarity. *New Journal of Physics*, 16(6):065009, 2014.

[16] Seth Zonies, Fumio Motegi, Yingsong Hao, and Geraldine Seydoux. Symmetry breaking and polarization of the c. elegans zygote by the polarity protein par-2. *Development*, 137(10):1669–1677, 2010.